# Analytical design of stretching-dominated truss lattices with tailored elasticity from transversely isotropic base materials

Qingping Ma [a,b,c], Lei Zhang [a,d], Junhao Ding [b], Shuo Qu [b], Jin Fu [e], Ming Wang Fu [e], Xu Song [b,*], Michael Yu Wang [a,c,f,*]

[a] Department of Mechanical and Aerospace Engineering, Hong Kong University of Science and Technology, Kowloon, Hong Kong, China
[b] Department of Mechanical and Automation Engineering, Chinese University of Hong Kong, Shatin, Hong Kong, China
[c] HKUST Shenzhen-Hong Kong Collaborative Innovation Research Institute, Futian, Shenzhen, China
[d] Meta Robotics Institute, Shanghai Jiao Tong University, Shanghai, China
[e] Department of Mechanical Engineering, Hong Kong Polytechnic University, Kowloon, Hong Kong, China
[f] Department of Mechanical and Aerospace Engineering, Monash University, Melbourne, Victoria, Australia

## HIGHLIGHTS

- Establish analytical homogenization formulas to determine the elastic constants of stretching-dominated truss lattices with transversely isotropic base materials.
- Propose an analytical approach to design elastically isotropic stretching-dominated truss lattices with transversely isotropic base materials.
- Develop traversal searching methods to obtain stretching-dominated truss lattices with tailored zero/negative Poisson's ratios and superior stiffness.
- Validate the effectiveness of the proposed design method incorporating material anisotropy through finite element analysis and experimental tests.

## GRAPHICAL ABSTRACT
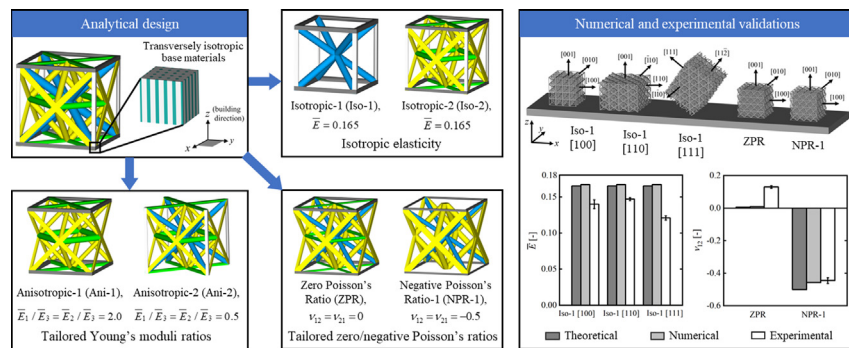
## ABSTRACT

Incorporating the process-induced material anisotropy into design framework of additively manufactured lattice structures is crucial to ensure the accuracy of design and analysis models. This work proposes an analytical approach to design stretching-dominated truss lattices with tailored elastic properties, including isotropic elasticity, tailored zero/negative Poisson's ratios, tailored Young's moduli ratios along specified directions. The transversely isotropic elasticity is adopted to represent the micro lase powder bed fusion (LPBF) process-induced anisotropy of base materials. The lattices are designed through combination of elementary bars with appropriate volume fractions. An analytical homogenization theory is established to determine elastic constants of combined lattices. An analytical design approach is proposed to obtain elastically isotropic truss lattices. A traversal searching is performed to determine ranges of Young's moduli, Poisson's ratios of combined lattices, and find most manufacturable ones with tailored Young's moduli ratios and Poisson's ratios. Finite element analysis reveals all designed lattices from anisotropic materials achieve better agreements to design targets than those designed from

---

\* Corresponding authors at: Department of Mechanical and Aerospace Engineering, Hong Kong University of Science and Technology, Kowloon, Hong Kong, China.
   *E-mail addresses:* xsong@cuhk.edu.hk (X. Song), michael.y.wang@monash.edu (M. Yu Wang).

isotropic materials, thus validating the superiority of the proposed method. The lattices with isotropic elasticity, tailored zero/negative Poisson's ratios are fabricated in stainless steel 316L via micro-LPBF, and quasi-static compression experiments are performed to further validate the proposed design approach.

## 1. Introduction

Truss lattices are a special class of periodic lattice structures, in which the primitive unit cell consists of a set of bars [1,2]. Truss lattices are known for their open-cell property, which is favourable for the liquid resin or metal powder based additive manufacturing (AM) [3–5], and mass and heat transfer related multifunctional applications [6–8]. Besides, truss lattices possess superior stiffness and strength to the earlier appearing open-cell stochastic foams with equal relative densities [1,9]. Depending on the deformation behaviours under external loads, truss lattices are classified as stretching-dominated and bending-dominated ones [10,11]. Typically, stretching-dominated truss lattices possess superior stiffness, yielding and buckling strength to bending-dominated ones at lower relative densities [10–13]. Accordingly, the design of stretching-dominated truss lattices with tailored mechanical properties is of practical significance.

Up to now, many efforts have been made to develop stretching-dominated truss lattices with tailored elastic properties, including isotropic elasticity, tailored zero/negative Poisson's ratios, tailored Young's moduli ratios along specified directions, in which the analytical and numerical methods are two main design approaches. Compared with the numerical method, the main advantages of the analytical method are the thorough understanding of the essence of design problems and significantly lower computational cost. An analytical homogenization theory is well established to determine the elastic constants of stretching-dominated truss lattices [14,15]. Based on this theory, a series of elastically isotropic stretching-dominated truss lattices are designed through combination of anisotropic three-dimensional (3D) cubic lattices with appropriate volume fractions [14–16], including simple cubic (SC), body-centered cubic (BCC), face-centered cubic (FCC). All combined lattices possess identical elastic moduli and approach 1/3 of the Hashin-Shtrikman stiffness upper bounds for 3D isotropic two-phase materials at low density limit [17,18]. Similarly, truss lattices can be analytically designed to achieve tailored Young's moduli ratios along specified directions through adjusting the cross-sectional radii and relative densities of the elementary bars [19,20], and tailored zero/negative Poisson's ratios through the re-entrant [21], chirality [22], anti-chirality [23] or rotating rigid mechanism [24] design strategies.

However, all the above-mentioned truss lattices related studies are based on the assumption of isotropic base materials, while the material anisotropy is generally inevitable in the layer-by-layer AM [25–28], thus leading to non-negligible discrepancies among the relevant theoretical, numerical and experimental results. Typically, the base materials fabricated by AM processes exhibit transversely isotropic elasticity [29,30], since materials are deposited, joined and solidified layer by layer to form 3D objects. The base materials possess nearly identical elastic properties within the horizontal plane, while the properties are different from those along the vertical direction [31]. Accordingly, several attempts were made to incorporate the material anisotropy into the structural design and analysis processes. Li et al. [32], Wang et al. [33] characterized the transverse isotropy of base materials via experimental tests on the additively manufactured tensile samples, and introduced the material anisotropy into the topology optimization

of cantilever beams, which resulted in nearly 10% improvement of their stiffness and strength than the optimized designs without consideration of material anisotropy. To further enlarge the design space and improve the mechanical properties, Jantos et al. [34], Yan et al. [35], Lu et al. [36] proposed several concurrent topology optimization frameworks, in which the microscale lattice structures were treated as homogenized anisotropic materials, and the elemental densities of macrostructures and orientations of anisotropic microstructures were optimized simultaneously. These works targeted on the design and optimization of macrostructures. Hereupon, Wu et al. [37], Sun et al. [38] introduced the transversely isotropic elasticity into the analysis of truss lattices, and concluded that the anisotropy model enabled more accurate predication of their mechanical properties. However, these analysis approaches were not integrated into design methods to tailor the mechanical properties of truss lattices with transversely isotropic base materials.

This paper aims to improve the design accuracy of AM fabricated truss lattices by incorporating the process-induced anisotropy of base materials. An analytical method is proposed to design stretching-dominated truss lattices with tailored elastic properties, including isotropic elasticity, tailored zero/negative Poisson's ratios, and tailored Young's moduli ratios along specified directions, in which the transversely isotropic elasticity model is adopted to represent the micro laser powder bed fusion (LPBF) process-induced anisotropy of the base materials. The lattices are designed through the combination of several groups of bars with appropriate volume fractions. An analytical homogenization theory is established to determine all elastic constants of the combined lattices. An analytical design approach is proposed to obtain elastically isotropic truss lattices with transversely isotropic base materials. Furthermore, a traversal searching method is developed to determine the ranges of Young's moduli, Poisson's ratios of combined lattices, and find the most manufacturable ones with tailored Young's moduli ratios and Poisson's ratios. The proposed stretching-dominated truss lattices with tailored zero/negative Poisson's ratios possess superior stiffness to their bending-dominated counterparts reported in previous studies. The elastic properties of the designed lattices are validated via numerical homogenization, which is implemented through the Timoshenko-Ehrenfest beam theory based finite element analysis (FEA). Besides, the designed lattices with unconventional properties of isotropic elasticity, tailored zero/negative Poisson's ratios are fabricated in stainless steel 316 L (SS316L) materials via micro-LPBF. Quasi-static compression test experiments are performed to further validate the proposed analytical design method. The proposed design and analysis method may contribute to the applications of lattices in the fields including lightweight and high-stiffness structures with isotropic elasticity, and bone implants with controllable elastic anisotropy.

## 2. Analytical design methods

### 2.1. Transversely isotropic base materials

Transversely isotropic base materials exhibit symmetric physical properties with regard to the axis normal to its plane of iso-

tropy. The materials possess identical properties along all directions within the plane of isotropy, while the property along the normal direction is different [31]. The constitutive relation of the materials is $\varepsilon^b = S^b \sigma^b$, in which the superscript $b$ denotes the base materials, $\varepsilon^b$, $S^b$, $\sigma^b$ denote the strain vector, compliance matrix, stress vector of the base materials, respectively, and are represented in matrix form with Voigt notation as:

$$
\boldsymbol{\varepsilon}^b = \begin{bmatrix} \varepsilon_1^b \\ \varepsilon_2^b \\ \varepsilon_3^b \\ \varepsilon_4^b \\ \varepsilon_5^b \\ \varepsilon_6^b \end{bmatrix}, \; \mathbf{S}^b = \begin{bmatrix} \frac{1}{E_1^b} & -\frac{v_{12}^b}{E_1^b} & -\frac{v_{13}^b}{E_1^b} & 0 & 0 & 0 \\ & \frac{1}{E_1^b} & -\frac{v_{13}^b}{E_1^b} & 0 & 0 & 0 \\ & & \frac{1}{E_3^b} & 0 & 0 & 0 \\ & sym & & \frac{1}{G_{13}^b} & 0 & 0 \\ & & & & \frac{1}{G_{13}^b} & 0 \\ & & & & & \frac{2(1+v_{12}^b)}{E_1^b} \end{bmatrix}, \; \boldsymbol{\sigma}^b = \begin{bmatrix} \sigma_1^b \\ \sigma_2^b \\ \sigma_3^b \\ \sigma_4^b \\ \sigma_5^b \\ \sigma_6^b \end{bmatrix},
$$

(1)

where the compliance matrix $\mathbf{S}^b$ includes five independent elastic constants: two independent Young's moduli $E_1^b$, $E_3^b$ along $x$, $z$ directions, one shear modulus $G_{13}^b$ within $x$-$z$ plane, and two independent Poisson's ratios $v_{12}^b$, $v_{13}^b$ corresponding to an extension along $y$, $z$ directions when a contraction is applied along $x$ direction, respectively. The Young's modulus of the transversely isotropic materials along an arbitrary direction with the unit vector of $\boldsymbol{n} = (n_1, n_2, n_3)$ is:

$$
E_n^b = 1 / \left[ \frac{1}{E_1^b} (n_1^2 + n_2^2)(n_1^2 + n_2^2 - 2v_{13}^b n_3^2) + \frac{1}{E_3^b} n_3^4 + \frac{1}{G_{13}^b} n_3^2 (n_1^2 + n_2^2) \right].
$$

(2)

The derivation details of Eq. (2) are shown in Appendix A.

The transversely isotropic elasticity of the micro-LPBF fabricated SS316L was calibrated through experimental tests on standard tensile samples fabricated along different directions. The five independent elastic constants are listed in Table 1, and the details of the calibration process are referred to our previous work [39].

## 2.2. Analytical design methods of truss lattices with tailored elasticity

This work focuses on orthorhombic truss lattices, whose unit cells possess reflectional symmetry regarding the three orthogonal middle planes. The constitutive bars are taken from the three cubic truss lattices of SC, BCC, FCC families, and the circular cross-section is adopted for all bars, as shown in Fig. 1. The main difference of the proposed method compared with the current methods based on isotropic base materials is that bars may possess different axial Young's moduli according to their building orientations. Given the transverse isotropy of the base materials, the constitutive bars are classified into five groups (I, II, III, IV, V), each of which possesses the same axial Young's modulus, as calculated from Eq. (2) and listed in Table 2. Accordingly, the bars within the same group are assigned with the same design variable, i.e., the same cross-sectional radius. To design truss lattices with tailored elastic properties, the analytical theory is developed based on the following assumptions:

**Table 1**
Elastic constants of SS316L materials fabricated by micro-LPBF.

| Property | $E_1^b$ [GPa] | $E_3^b$ [GPa] | $G_{13}^b$ [GPa] | $v_{12}^b$ [−] | $v_{13}^b$ [−] |
|---|---|---|---|---|---|
| Value | 189.31 | 173.71 | 75.02 | 0.24 | 0.29 |
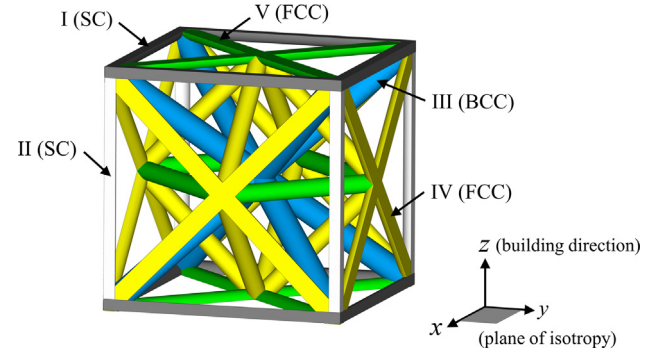


**Fig. 1.** The five groups of bars within the cubic truss lattices of SC, BCC, FCC families, in which each colour represents an individual group of bars with the same axial Young's modulus.

**Table 2**
Axial Young's moduli of the five groups of bars within the three cubic truss lattices.

| Cubic lattice | Unit vector ($\mathbf{n}$) | Axial Young's modulus ($E$) | Group of bars |
|---|---|---|---|
| SC | (1, 0, 0) (0, 1, 0) | $E_I = E_1^b$ | I |
| | (0, 0, 1) | $E_{II} = E_3^b$ | II |
| BCC | (1, 1, 1) (1, 1, −1) (1, −1, 1) (−1, 1, 1) | $E_{III} = 9 / \left[ \frac{4}{E_1^b}(1 - v_{13}^b) + \frac{1}{E_3^b} + \frac{2}{G_{13}^b} \right]$ | III |
| FCC | (1, 0, 1) (1, 0, −1) (0, 1, 1) (0, 1, −1) | $E_{IV} = 4 / \left[ \frac{1}{E_1^b}(1 - 2v_{13}^b) + \frac{1}{E_3^b} + \frac{1}{G_{13}^b} \right]$ | IV |
| | (1, 1, 0) (1, −1, 0) | $E_V = E_1^b$ | V |

1. The base materials are linear elastic, homogeneous, and transversely isotropic.
2. All bars undergo small deformation.
3. All nodes are pin-jointed; all bars are infinitely extended; and the combined lattices exhibit stretching-dominated deformation behaviours.

Under this circumstance, all constitutive bars only bear uniaxial loads along axial directions, while the transverse, shear and bending loads are small. Therefore, the proposed analytical design model only involves the axial Young's modulus of each constitutive bar.

The macroscopic constitutive equation of a truss lattice is $\sigma = C\varepsilon$, in which $\sigma$, $\varepsilon$, $\mathbf{C}$ are the homogenized stress vector, strain vector, elasticity matrix of the lattice, and are denoted in matrix form with the Voigt notation as [16]:

$$
\boldsymbol{\sigma} = \begin{bmatrix} \sigma_1 \\ \sigma_2 \\ \sigma_3 \\ \sigma_4 \\ \sigma_5 \\ \sigma_6 \end{bmatrix}, \; \mathbf{C} = \begin{bmatrix} C_{11} & C_{12} & C_{13} & C_{14} & C_{15} & C_{16} \\ & C_{22} & C_{23} & C_{24} & C_{25} & C_{26} \\ & & C_{33} & C_{34} & C_{35} & C_{36} \\ & sym & & C_{44} & C_{45} & C_{46} \\ & & & & C_{55} & C_{56} \\ & & & & & C_{66} \end{bmatrix}
$$

$$
= \begin{bmatrix} c_{1111} & c_{1112} & c_{1113} & c_{1114} & c_{1115} & c_{1116} \\ & c_{2222} & c_{2233} & c_{2223} & c_{2213} & c_{2212} \\ & & c_{3333} & c_{3323} & c_{3313} & c_{3312} \\ & sym & & c_{2323} & c_{2313} & c_{2312} \\ & & & & c_{1313} & c_{1312} \\ & & & & & c_{1212} \end{bmatrix}, \; \boldsymbol{\varepsilon} = \begin{bmatrix} \varepsilon_1 \\ \varepsilon_2 \\ \varepsilon_3 \\ \varepsilon_4 \\ \varepsilon_5 \\ \varepsilon_6 \end{bmatrix},
$$

(3)

where the components of the elasticity tensor of a stretching-dominated truss lattice are obtained from an established homogenization theory as [14–16]:

$$c_{pqrs} = \sum_{i \in UC} \rho^i E_i^b n_p^i n_q^i n_r^i n_s^i, \quad (p, q, r, s = 1, 2, 3), \tag{4}$$

where $UC$ denotes the assembly of bars contained within the lattice unit cell; $n^i$ represents the unit axial vector of bar $i$, $n_p^i$ denotes the $p$-th component of $n^i$; $E_i^b$ denotes the Young's modulus of base materials along $\boldsymbol{n}^i$ direction; $\rho^i$ denotes the volume fraction of the $i$-th set of bars, and satisfies:

$$\sum_{i \in UC} \rho^i = \bar{\rho}, \tag{5}$$

where $\bar{\rho}$ denotes the relative density of the lattice. To ensure stretching-dominated deformation behaviours, the axial force equilibrium equation for all bars connecting at node $J$ needs to be satisfied:

$$\sum_{i \in S(J)} A^i E_i^b n_p^i n_q^i \boldsymbol{n}^i = \boldsymbol{0}, \quad (p, q = 1, 2, 3), \tag{6}$$

in which $A$ represents the cross-sectional area, $S(J)$ represents the assembly of bars that connect at node $J$.

### 2.2.1. Design of truss lattices with isotropic elasticity

For an elastically isotropic truss lattice, the elasticity matrix states:

$$\mathbf{C} = \frac{E}{1+v} \begin{bmatrix} \frac{1-v}{1-2v} & \frac{v}{1-2v} & \frac{v}{1-2v} & 0 & 0 & 0 \\ & \frac{1-v}{1-2v} & \frac{v}{1-2v} & 0 & 0 & 0 \\ & & \frac{1-v}{1-2v} & 0 & 0 & 0 \\ & sym & & 0.5 & 0 & 0 \\ & & & & 0.5 & 0 \\ & & & & & 0.5 \end{bmatrix}, \tag{7}$$

where $E$, $v$ denote the Young's modulus, Poisson's ratio of the lattice. Through equating the corresponding components of the elasticity matrix in Eqs. (3), (4) and those in Eq. (7), the criteria for a stretching-dominated truss lattice to achieve isotropic elasticity are obtained as:

$$\sum_{i \in UC} \rho^i E_i^b \left(n_p^i\right)^2 n_q^i n_r^i = 0, \quad (p, q, r = 1, 2, 3; q \neq r), \tag{8a}$$

$$\sum_{i \in UC} \rho^i E_i^b \left(n_p^i\right)^2 = \frac{1}{3} \sum_{i \in UC} \rho^i E_i^b, \quad (p = 1, 2, 3), \tag{8b}$$

$$\sum_{i \in UC} \rho^i E_i^b \left(n_p^i\right)^4 = \frac{1}{5} \sum_{i \in UC} \rho^i E_i^b, \quad (p = 1, 2, 3). \tag{8c}$$

For an orthorhombic lattice, Eq. (8a) is always satisfied, and Eqs. (8b)~(8c) should be further satisfied through combination of the five groups of bars with appropriate volume fractions. Once the isotropic elasticity is reached, the elastic properties of the combined lattice are obtained as [14–16]:

$$E = \frac{1}{6} \sum_{i \in UC} \rho^i E_i^b, \quad v = 0.25. \tag{9}$$

Given the transverse isotropy of the base materials, Eqs. (8b)~(8c) represent four independent linear equations. Combining the four equations with Eq. (5) yields the following linear equation system to determine the volume fractions of the five groups of bars for the combined lattices to obtain isotropic elasticity:

$$\begin{bmatrix} 1 & 1 & 1 & 1 & 1 \\ \frac{3}{10}E_I & -\frac{1}{5}E_{II} & -\frac{4}{45}E_{III} & -\frac{3}{40}E_{IV} & \frac{1}{20}E_V \\ -\frac{1}{5}E_I & \frac{4}{5}E_{II} & -\frac{4}{45}E_{III} & \frac{1}{20}E_{IV} & -\frac{1}{5}E_V \\ \frac{1}{6}E_I & -\frac{1}{3}E_{II} & 0 & -\frac{1}{12}E_{IV} & \frac{1}{6}E_V \\ -\frac{1}{3}E_I & \frac{2}{3}E_{II} & 0 & \frac{1}{6}E_{IV} & -\frac{1}{3}E_V \end{bmatrix} \begin{bmatrix} \rho^I \\ \rho^{II} \\ \rho^{III} \\ \rho^{IV} \\ \rho^V \end{bmatrix} = \begin{bmatrix} \bar{\rho} \\ 0 \\ 0 \\ 0 \\ 0 \end{bmatrix}. \tag{10}$$

With the five Young's moduli given in Table 2, the rank of the coefficient matrix in Eq. (10) is analytically calculated to be 4, implying the existence of infinite solutions. The general solutions of the linear equation system in Eq. (10) are analytically calculated as:

$$\begin{bmatrix} \rho^I \\ \rho^{II} \\ \rho^{III} \\ \rho^{IV} \\ \rho^V \end{bmatrix} = \begin{bmatrix} -\frac{16E_I E_{II} E_{III} - 9E_I E_{II} E_{IV} + 8E_{II} E_{III} E_{IV}}{2E_{IV}(9E_I E_{II} + 2E_I E_{III} + 4E_{II} E_{III})} \\ -\frac{E_I(16E_I E_{III} - 9E_I E_{IV} + 8E_{III} E_{IV})}{4E_{IV}(9E_I E_{II} + 2E_I E_{III} + 4E_{II} E_{III})} \\ -\frac{9E_I(8E_I E_{II} + E_I E_{IV} + 6E_{II} E_{IV})}{4E_{IV}(9E_I E_{II} + 2E_I E_{III} + 4E_{II} E_{III})} \\ \frac{2E_I}{E_{IV}} \\ 1 \end{bmatrix} \rho^V$$

$$+ \begin{bmatrix} \frac{4E_{II} E_{III} \bar{\rho}}{9E_I E_{II} + 2E_I E_{III} + 4E_{II} E_{III}} \\ \frac{2E_I E_{III} \bar{\rho}}{9E_I E_{II} + 2E_I E_{III} + 4E_{II} E_{III}} \\ \frac{9E_1 E_{II} \bar{\rho}}{9E_I E_{II} + 2E_I E_{III} + 4E_{II} E_{III}} \\ 0 \\ 0 \end{bmatrix}, \tag{11}$$

where the variable $\rho^V$ can vary independently to yield a series of feasible solutions for the combined lattices to obtain isotropic elasticity, as long as $0 \leqslant \rho^i \leqslant \bar{\rho}$, $(i = I, II, III, IV, V)$. The elastic constants of the elastically isotropic combined lattices in Eq. (9) are normalized as:

$$\bar{E} = \frac{E}{\bar{\rho} E_I} = \frac{5}{2\left(9\frac{E_I}{E_{III}} + 2\frac{E_I}{E_{II}} + 4\right)}, \quad v = 0.25. \tag{12}$$

Eq. (12) shows that once the isotropic elasticity is obtained, the lattices possess the same Young's modulus, whose value only depends on the three axial Young's moduli $E_I$, $E_{II}$, $E_{III}$, and identical Poisson's ratio of 0.25. The relations between the volume fractions and cross-sectional radii ($R_I$, $R_{II}$, $R_{III}$, $R_{IV}$, $R_V$) of the five groups of bars are formulated as:

$$\rho^I = \frac{2\pi R_I^2}{D^2}, \quad \rho^{II} = \frac{\pi R_{II}^2}{D^2}, \quad \rho^{III} = \frac{4\sqrt{3}\pi R_{III}^2}{D^2}, \quad \rho^{IV} = \frac{8\sqrt{2}\pi R_{IV}^2}{D^2}, \quad \rho^V = \frac{4\sqrt{2}\pi R_V^2}{D^2}, \tag{13}$$

in which $D$ denotes the unit cell size of the lattice. Given the volume fractions of the five groups of bars, the corresponding cross-sectional radii are determined by Eq. (13).

Among all feasible solutions in Eq. (11), there are two special ones. The first one includes only the bars within SC and BCC truss lattices ($\rho^{IV} = \rho^V = 0$):

$$\begin{bmatrix} \rho^I \\ \rho^{II} \\ \rho^{III} \\ \rho^{IV} \\ \rho^V \end{bmatrix} = \frac{\bar{\rho}}{9E_I E_{II} + 2E_I E_{III} + 4E_{II} E_{III}} \begin{bmatrix} 4E_{II} E_{III} \\ 2E_I E_{III} \\ 9E_I E_{II} \\ 0 \\ 0 \end{bmatrix}, \tag{14}$$

while the other one includes only the bars within SC and FCC lattices ($\rho^{III} = 0$):

$$\begin{bmatrix} \rho^I \\ \rho^{II} \\ \rho^{III} \\ \rho^{IV} \\ \rho^V \end{bmatrix} = \frac{\bar{\rho}}{9E_IE_{II} + 2E_IE_{III} + 4E_{II}E_{III}}$$

$$\times \begin{bmatrix} 4E_{II}E_{III} - \dfrac{2E_{II}(16E_IE_{II}E_{III} - 9E_IE_{II}E_{IV} + 8E_{II}E_{III}E_{IV})}{8E_IE_{II} + E_IE_{IV} + 6E_{II}E_{IV}} \\ 2E_IE_{III} - \dfrac{E_IE_{II}(16E_IE_{III} - 9E_IE_{IV} + 8E_{III}E_{IV})}{8E_IE_{II} + E_IE_{IV} + 6E_{II}E_{IV}} \\ 0 \\ \dfrac{8E_IE_{II}(9E_IE_{II} + 2E_IE_{III} + 4E_{II}E_{III})}{8E_IE_{II} + E_IE_{IV} + 6E_{II}E_{IV}} \\ \dfrac{4E_IE_{IV}(9E_IE_{II} + 2E_IE_{III} + 4E_{II}E_{III})}{8E_IE_{II} + E_IE_{IV} + 6E_{II}E_{IV}} \end{bmatrix}. \quad (15)$$

The two special lattices are investigated in detail in this work, as shown in Fig. 2, in which Isotropic-1 (Iso-1), Isotropic-2 (Iso-2) denote the elastically isotropic SC-BCC, SC-FCC combined lattices with $\bar{\rho} = 10\%$, respectively. The normalized Young's moduli of the lattices and normalized cross-sectional radii of the five groups of bars are listed in Table 3. The Iso-1, Iso-2 lattices possess identical normalized Young's moduli $\bar{E} = 0.165$, and Poisson's ratio $v = 0.25$. To further clarify the superiority of the proposed design method considering material anisotropy, the lattices are re-designed based on the assumption of isotropic base materials with the Young's modulus $E_1^b$ and Poisson's ratio $v_{12}^b$, which are also included in Table 3. The elastic constants of the designed lattices will be investigated via FEA based numerical homogenization and the errors away from the design targets will be evaluated, in which the base materials are the realistic transversely isotropic SS316L materials (Table 1).

### 2.2.2. Design of truss lattices with tailored Young's moduli ratios

Given the transverse isotropy of the base materials, the elasticity matrix of a stretching-dominated orthorhombic truss lattice is derived from Eqs. (3)~(4) as:

$$\mathbf{C} = \begin{pmatrix} C_{11} & C_{12} & C_{13} & 0 & 0 & 0 \\ & C_{11} & C_{13} & 0 & 0 & 0 \\ & & C_{33} & 0 & 0 & 0 \\ & sym & & C_{44} & 0 & 0 \\ & & & & C_{44} & 0 \\ & & & & & C_{66} \end{pmatrix}, \quad (16)$$

with

$$C_{11} = \tfrac{1}{2}\rho^I E_I + \tfrac{1}{9}\rho^{III}E_{III} + \tfrac{1}{8}\rho^{IV}E_{IV} + \tfrac{1}{4}\rho^V E_V, \; C_{33} = \rho^{II}E_{II} + \tfrac{1}{9}\rho^{III}E_{III} + \tfrac{1}{4}\rho^{IV}E_{IV},$$
$$C_{12} = C_{66} = \tfrac{1}{9}\rho^{III}E_{III} + \tfrac{1}{4}\rho^V E_V, \; C_{13} = C_{44} = \tfrac{1}{9}\rho^{III}E_{III} + \tfrac{1}{8}\rho^{IV}E_{IV}. \quad (17)$$

Correspondingly, the compliance matrix of the lattice is derived as:

$$\mathbf{S} = \mathbf{C}^{-1} = \begin{pmatrix} S_{11} & S_{12} & S_{13} & 0 & 0 & 0 \\ & S_{11} & S_{13} & 0 & 0 & 0 \\ & & S_{33} & 0 & 0 & 0 \\ & sym & & S_{44} & 0 & 0 \\ & & & & S_{44} & 0 \\ & & & & & S_{66} \end{pmatrix}, \quad (18)$$

with

$$S_{11} = \frac{-C_{13}^2 + C_{11}C_{33}}{(C_{11}-C_{12})(-2C_{13}^2 + C_{11}C_{33} + C_{12}C_{33})}, \; S_{33} = \frac{C_{11}+C_{12}}{-2C_{13}^2 + C_{11}C_{33} + C_{12}C_{33}},$$
$$S_{12} = \frac{C_{13}^2 - C_{12}C_{33}}{(C_{11}-C_{12})(-2C_{13}^2 + C_{11}C_{33} + C_{12}C_{33})}, \; S_{13} = -\frac{C_{13}}{-2C_{13}^2 + C_{11}C_{33} + C_{12}C_{33}}, \quad (19)$$
$$S_{44} = \frac{1}{C_{13}}, \; S_{66} = \frac{1}{C_{12}}.$$

The Young's moduli are derived from Eqs. (17) and (19) as:

$$E_1 = E_2 = \frac{1}{S_{11}} = \frac{(C_{11}-C_{12})(-2C_{13}^2 + C_{11}C_{33} + C_{12}C_{33})}{-C_{13}^2 + C_{11}C_{33}},$$
$$E_3 = \frac{1}{S_{33}} = \frac{-2C_{13}^2 + C_{11}C_{33} + C_{12}C_{33}}{C_{11}+C_{12}}, \quad (20)$$

where $E_1$, $E_2$, $E_3$ denote the Young's moduli along [100], [010], [001] directions, respectively.
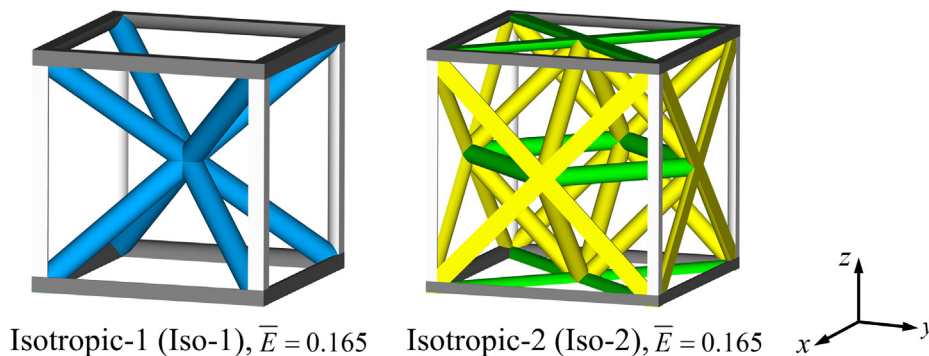


**Fig. 2.** Elastically isotropic SC-BCC (Iso-1), SC-FCC (Iso-2) combined truss latices ($\bar{\rho} = 10\%$).

**Table 3**
Normalized Young's moduli of elastically isotropic truss lattices ($\bar{\rho} = 10\%$) designed from transversely isotropic base materials and isotropic base materials, and normalized cross-sectional radii of the five groups of bars.

| Lattice | | Design target | $R_1/D\ [-]$ | $R_2/D\ [-]$ | $R_3/D\ [-]$ | $R_4/D\ [-]$ | $R_5/D\ [-]$ |
|---|---|---|---|---|---|---|---|
| Transversely isotropic base materials | Isotropic-1 (Iso-1) | $\bar{E} = 0.165$ | $6.48 \times 10^{-2}$ | $6.77 \times 10^{-2}$ | $5.22 \times 10^{-2}$ | 0 | 0 |
| | Isotropic-2 (Iso-2) | $\bar{E} = 0.165$ | $4.58 \times 10^{-2}$ | $4.78 \times 10^{-2}$ | 0 | $3.87 \times 10^{-2}$ | $3.85 \times 10^{-2}$ |
| Isotropic base materials | Isotropic-1 (Iso-1) | $\bar{E} = 0.167$ | $6.51 \times 10^{-2}$ | $6.51 \times 10^{-2}$ | $5.25 \times 10^{-2}$ | 0 | 0 |
| | Isotropic-2 (Iso-2) | $\bar{E} = 0.167$ | $4.61 \times 10^{-2}$ | $4.61 \times 10^{-2}$ | 0 | $3.87 \times 10^{-2}$ | $3.87 \times 10^{-2}$ |

Eqs. (17), (20) imply that the Young's moduli are nonlinear functions of the volume fractions of the five groups of bars. Therefore, it is not straightforward to form a set of linear equations to design truss lattices with tailored Young's moduli ratios. To address this design problem, a traversal searching is performed to determine the ranges of the three Young's moduli of orthorhombic truss lattices, in which the volume fractions of the five groups of bars vary within the feasible ranges, i.e., $0 \leqslant \rho^i \leqslant \bar{\rho}$, $(i = I, II, III, IV, V)$, and they all satisfy the relation in Eq. (5). The cross-sectional radii of the five groups of bars are determined by Eq. (13). Based on the ranges of the three Young's moduli obtained from traversal searching, all possible lattices with tailored moduli ratios along specified directions are achieved, among which the most manufacturable ones are identified and selected for experimental validation. The following two criteria are employed to determine the most manufacturable lattices:

1. At least three values among the five cross-sectional radii are non-zero.
2. Among all feasible combined lattices satisfying the first criterion, the lattice with the smallest value of coefficient of variation ($R_{cv}$) of all the non-zero radii is the most manufacturable one, in which:

$$R_{cv} = \frac{\sqrt{\frac{1}{Z}\left[(R_1 - R_{avg})^2 + (R_2 - R_{avg})^2 + \ldots + (R_Z - R_{avg})^2\right]}}{R_{avg}}, \quad (21)$$

where $R_1, \ldots, R_Z$ denote the non-zero radii, whose average value is represented as $R_{avg}$.

The traversal searching reveals the ranges of the three normalized Young's moduli as $0 < \bar{E}_1 = \bar{E}_2 < 0.50$, and $0 < \bar{E}_3 < 0.91$, as illustrated in Fig. 3. The A₁ lattice possesses nearly zero Young's moduli along [100], [010], [001] directions, and much larger modulus along [111] direction, due to its very thin bars along [100], [010], [001] directions and significantly thicker bars along [111] direction. The A₂ lattice possesses thick bars along [100] and [010] directions, while very thin bars along the remaining directions, therefore its normalized modulus $\bar{E}_1$ reaches the maximum among all lattices, with a value of 0.50. Similarly, the A₃ lattice possesses the maximal modulus $\bar{E}_3$ among all lattices due to its thick bars along [001] direction, with a value of 0.91. The larger value of maximal modulus $\bar{E}_3$ is primarily attributed to the larger cross-sectional radii of vertical bars within A₃ lattice. In this work, we present two representative truss lattices with tailored moduli ratios along [100], [010], [001] directions, including Anisotropic-1 (Ani-1) and Anisotropic-2 (Ani-2) lattices with the Young's moduli ratios ($\bar{E}_1/\bar{E}_3 = \bar{E}_2/\bar{E}_3$) of 2.0 and 0.5, respectively, as illustrated in Fig. 4. The relative density is taken as $\bar{\rho} = 10\%$, and the normalized Young's moduli and normalized cross-sectional radii of the five groups of bars are listed in Table 4. Similarly, the lattices are re-designed based on the assumption of isotropic base materials with the Young's modulus $E_1^b$ and Poisson's ratio $v_{12}^b$ for comparison, and are also included in Table 4.

### 2.2.3. Design of truss lattices with tailored Poisson's ratios

The Poisson's ratios of stretching-dominated orthorhombic truss lattices are derived from Eqs. (19)–(20) as:
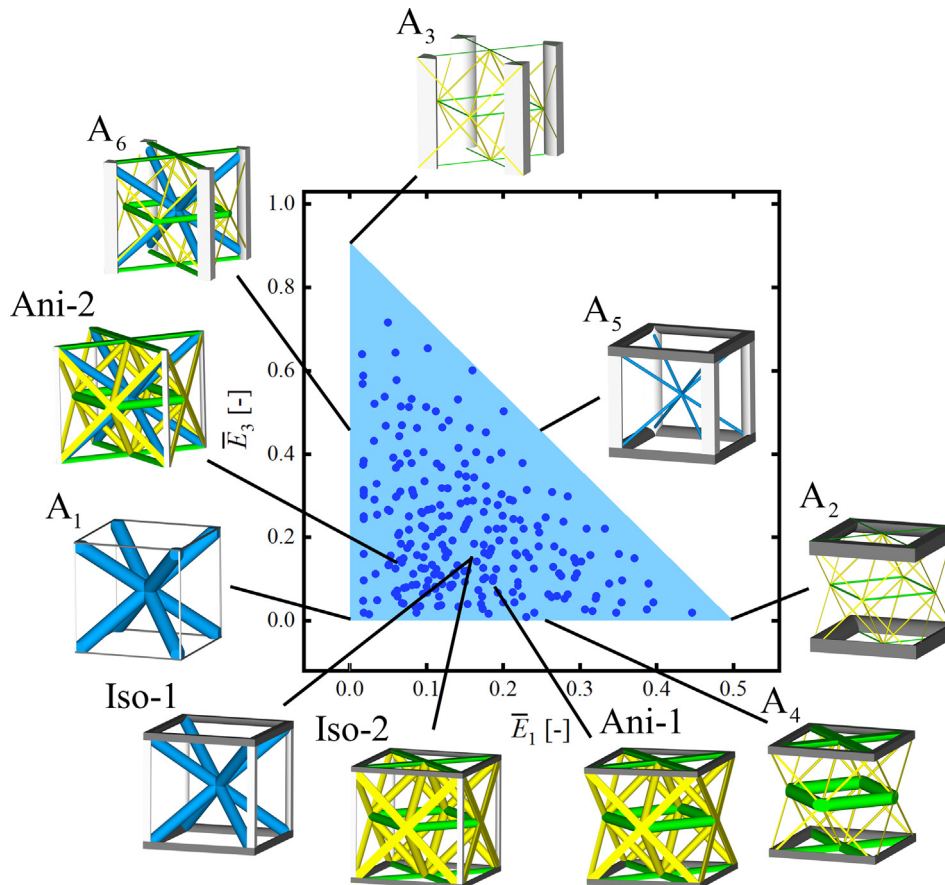


**Fig. 3.** Ranges of normalized Young's moduli $\bar{E}_1$, $\bar{E}_3$ of orthorhombic truss lattices with different topological configurations.
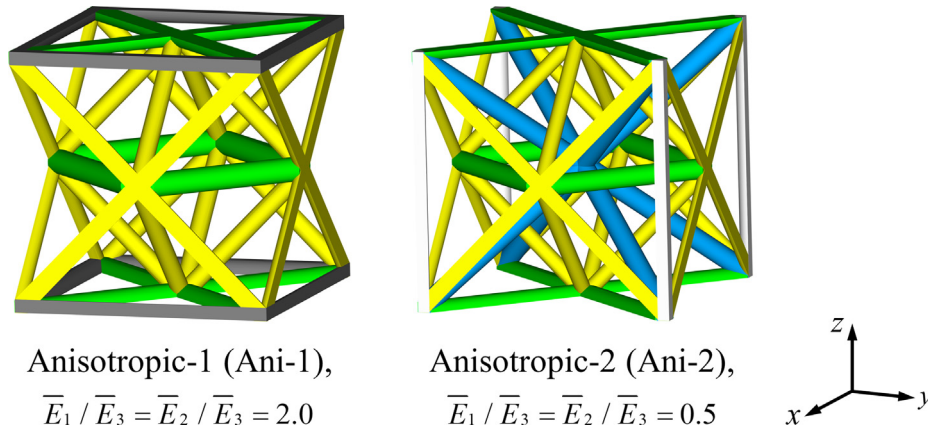
**Fig. 4.** Truss lattices with tailored Young's moduli ratios along specified directions ($\bar{\rho} = 10\%$).

**Table 4**
Normalized Young's moduli of truss lattices with tailored moduli ratios ($\bar{\rho} = 10\%$) designed from transversely isotropic base materials and isotropic base materials, and normalized cross-sectional radii of the five groups of bars.

| Lattice | | Design target | $R_1/D$ [−] | $R_2/D$ [−] | $R_3/D$ [−] | $R_4/D$ [−] | $R_5/D$ [−] |
|---|---|---|---|---|---|---|---|
| Transversely isotropic base materials | Anisotropic-1 (Ani-1) | $\bar{E}_1 = \bar{E}_2 = 0.184,$ $\bar{E}_3 = 0.092,$ $\frac{\bar{E}_1}{\bar{E}_3} = \frac{\bar{E}_2}{\bar{E}_3} = 2.0,$ | $5.12 \times 10^{-2}$ | 0 | 0 | $3.54 \times 10^{-2}$ | $4.68 \times 10^{-2}$ |
| | Anisotropic-2 (Ani-2) | $\bar{E}_1 = \bar{E}_2 = 0.065,$ $\bar{E}_3 = 0.130,$ $\frac{\bar{E}_1}{\bar{E}_3} = \frac{\bar{E}_2}{\bar{E}_3} = 0.5,$ | 0 | $4.55 \times 10^{-2}$ | $3.95 \times 10^{-2}$ | $2.98 \times 10^{-2}$ | $3.97 \times 10^{-2}$ |
| Isotropic base materials | Anisotropic-1 (Ani-1) | $\bar{E}_1 = \bar{E}_2 = 0.171,$ $\bar{E}_3 = 0.086,$ $\frac{\bar{E}_1}{\bar{E}_3} = \frac{\bar{E}_2}{\bar{E}_3} = 2.0,$ | $4.72 \times 10^{-2}$ | 0 | 0 | $3.35 \times 10^{-2}$ | $5.09 \times 10^{-2}$ |
| | Anisotropic-2 (Ani-2) | $\bar{E}_1 = \bar{E}_2 = 0.064,$ $\bar{E}_3 = 0.127,$ $\frac{\bar{E}_1}{\bar{E}_3} = \frac{\bar{E}_2}{\bar{E}_3} = 0.5,$ | 0 | $4.37 \times 10^{-2}$ | $4.18 \times 10^{-2}$ | $2.95 \times 10^{-2}$ | $3.75 \times 10^{-2}$ |

$$v_{12} = v_{21} = -S_{12}E_1 = \frac{C_{13}^2 - C_{12}C_{33}}{C_{13}^2 - C_{11}C_{33}},$$

$$v_{13} = v_{23} = -S_{13}E_1 = \frac{C_{13}(C_{11} - C_{12})}{-C_{13}^2 + C_{11}C_{33}}, \quad (22)$$

$$v_{31} = v_{32} = -S_{13}E_3 = \frac{C_{13}}{C_{11} + C_{12}},$$

where $v_{ij}$ denotes the Poisson's ratio corresponding to an extension in the $j$-th direction when the lattice is subjected to a contraction in the $i$-th direction. Similarly, the Poisson's ratios are nonlinear functions of the volume fractions of the five groups of bars. Thus, the traversal searching method introduced in Section 2.2.2 is adopted again to design stretching-dominated truss lattices with tailored Poisson's ratios. The traversal searching reveals the ranges of the six Poisson's ratios of orthorhombic truss lattices as $-1.0 < v_{12} = v_{21} < 1.0$, $0 < v_{13} = v_{23} < 1.0$, $0 < v_{31} = v_{32} < 1.0$, as illustrated in Fig. 5. Herein, six representative lattices (P$_1$, P$_2$, ..., P$_6$) with extreme values of Poisson's ratios are shown, all of which possess very thin bars along certain directions, and thick bars along the remaining directions. The two Poisson's ratios within $x$-$y$ plane ($v_{12}$, $v_{21}$) of the lattices may be negative, zero, or positive, while the other four ones are always positive. Accordingly, three representative lattices with tailored zero/negative Poisson's ratios within $x$-$y$ plane are obtained, as illustrated in Fig. 6, including Zero Poisson's Ratio (ZPR), Negative Poisson's Ratio-1 (NPR-1), Negative Poisson's Ratio-2 (NPR-2) lattices with tailored Poisson's ratios ($v_{12}$, $v_{21}$) of 0, −0.5, −0.8, respectively. The relative density of the lattices is $\bar{\rho} = 10\%$, the Poisson's ratios within $x$-$y$ plane and normalized cross-sectional

radii of the five groups of bars are listed in Table 5. The re-designed lattices based on the assumption of isotropic base materials with the Young's modulus $E_1^b$ and Poisson's ratio $v_{12}^b$ are also listed in Table 5 for comparison. The normalized Young's moduli of the proposed stretching-dominated lattices are compared with their bending-dominated counterparts reported in previous studies [21–23], as shown in Fig. 7, which illustrates that the proposed lattices outperform their bending-dominated counterparts in stiffness significantly.

## 3. FEA validation

### 3.1. FEA methods

In this work, a linear elastic FEA based numerical homogenization framework is adopted to validate the elastic properties of the designed lattices, using commercial software ABAQUS™ 2021. To compute the elastic constants of the lattices, six load cases are applied to the unit cell [40], including three uniaxial strain cases ($\varepsilon^{(1)} = [1, 0, 0, 0, 0, 0]^T$, $\varepsilon^{(2)} = [0, 1, 0, 0, 0, 0]^T$, $\varepsilon^{(3)} = [0, 0, 1, 0, 0, 0]^T$), and three pure shear cases ($\varepsilon^{(4)} = [0, 0, 0, 1, 0, 0]^T$, $\varepsilon^{(5)} = [0, 0, 0, 0, 1, 0]^T$, $\varepsilon^{(6)} = [0, 0, 0, 0, 0, 1]^T$). In linear elastic FEA, the magnitudes of testing strains do not affect the calculated elastic constants. Therefore, all six load cases employ the unit strain for simplicity. The ABAQUS B31 beam element, a 3D two-node linear beam element based on the classical Timoshenko-Ehrenfest beam
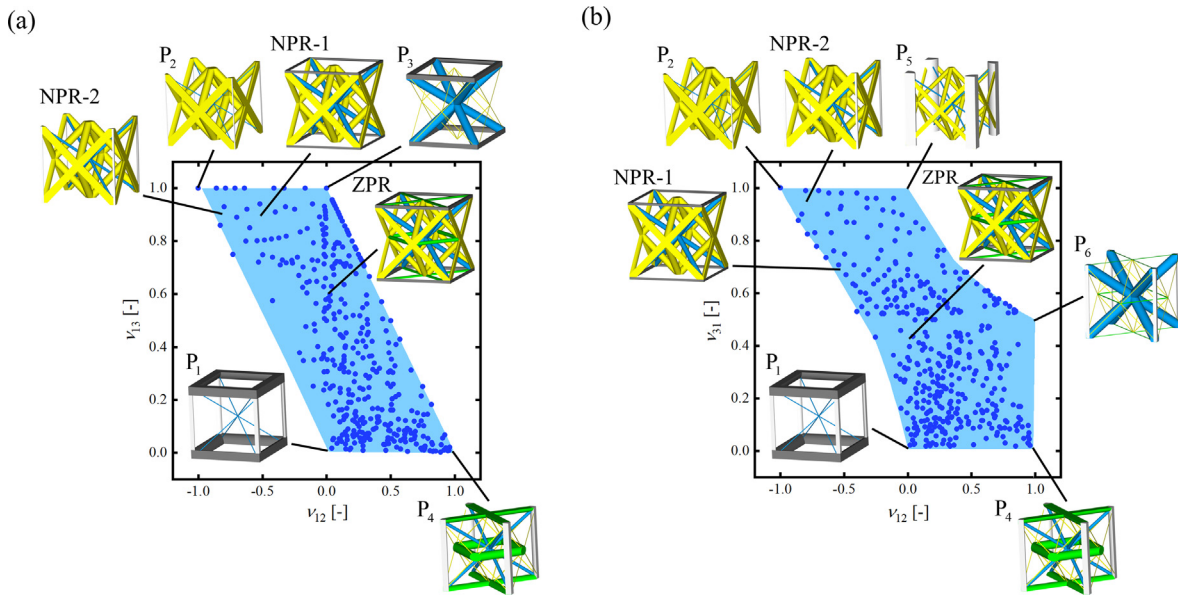
**Fig. 5.** Ranges of Poisson's ratios: (a) $v_{13}$ versus $v_{12}$, (b) $v_{31}$ versus $v_{12}$, of orthorhombic truss lattices with different topological configurations.



Zero Poisson's Ratio (ZPR),
$V_{12} = V_{21} = 0$

Negative Poisson's Ratio-1 (NPR-1),
$V_{12} = V_{21} = -0.5$

Negative Poisson's Ratio-2 (NPR-2),
$V_{12} = V_{21} = -0.8$
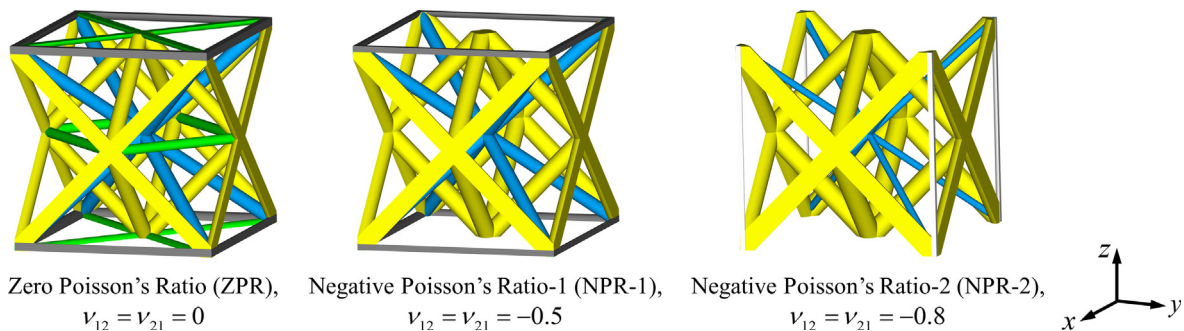
**Fig. 6.** Truss lattices with tailored zero/negative Poisson's ratios within *x-y* plane ($\bar{\rho} = 10\%$).

**Table 5**
Poisson's ratios within *x-y* plane of truss lattices with tailored Poisson's ratios ($\bar{\rho} = 10\%$) designed from transversely isotropic base materials and isotropic base materials, and normalized cross-sectional radii of the five groups of bars.

| Lattice | | Design target | $R_1/D$ [$-$] | $R_2/D$ [$-$] | $R_3/D$ [$-$] | $R_4/D$ [$-$] | $R_5/D$ [$-$] |
|---|---|---|---|---|---|---|---|
| Transversely isotropic base materials | Zero Poisson's Ratio (ZPR) | $v_{12} = 0$ | $3.89 \times 10^{-2}$ | 0 | $3.42 \times 10^{-2}$ | $3.90 \times 10^{-2}$ | $2.49 \times 10^{-2}$ |
| | Negative Poisson's Ratio-1 (NPR-1) | $v_{12} = -0.5$ | $2.96 \times 10^{-2}$ | 0 | $3.25 \times 10^{-2}$ | $4.49 \times 10^{-2}$ | 0 |
| | Negative Poisson's Ratio-2 (NPR-2) | $v_{12} = -0.8$ | 0 | $2.52 \times 10^{-2}$ | $1.73 \times 10^{-2}$ | $5.07 \times 10^{-2}$ | 0 |
| Isotropic base materials | Zero Poisson's Ratio (ZPR) | $v_{12} = 0$ | $8.56 \times 10^{-2}$ | $3.99 \times 10^{-2}$ | 0 | $3.44 \times 10^{-2}$ | $1.98 \times 10^{-2}$ |
| | Negative Poisson's Ratio-1 (NPR-1) | $v_{12} = -0.5$ | 0 | $4.72 \times 10^{-2}$ | $2.14 \times 10^{-2}$ | $4.83 \times 10^{-2}$ | 0 |
| | Negative Poisson's Ratio-2 (NPR-2) | $v_{12} = -0.8$ | $1.78 \times 10^{-2}$ | 0 | $1.79 \times 10^{-2}$ | $5.06 \times 10^{-2}$ | 0 |

theory, is employed for FEA. Each bar is meshed with at least 100 elements, and the axial Young's moduli in Table 2 are assigned to the corresponding groups of bars. The cross-sectional properties, including the area and second moments of area, are calculated from the cross-sectional radii and assigned to the corresponding groups of bars. Due to the unit cell's reflectional symmetry regarding the three orthogonal middle planes, the 1/8 unit cell is employed for analysis [41]. The symmetric/anti-symmetric boundary conditions are imposed on the three middle planes, and the periodic boundary conditions are simplified and imposed on the other three end planes [41]. The terms of the elasticity matrix in Eq. (3) are obtained from macroscopic stresses under the six load cases, which are evaluated by the average stress theorem [23,42].

The compliance matrix is calculated as the inverse of the elasticity matrix, from which the three axial Young's moduli ($E_1$, $E_2$, $E_3$) and six Poisson's ratios ($v_{12}$, $v_{21}$, $v_{13}$, $v_{31}$, $v_{23}$, $v_{32}$) are obtained. The details for implementing the FEA workflow are referred to our previous work [43].

To illustrate the tailored zero/negative Poisson's ratios within *x-y* plane, an additional FEA is performed to investigate the deformation responses of ZPR, NPR-1, NPR-2 lattices under uniaxial stress loading along *x* direction. Along *y*, *z* directions of the lattices, free extension or contraction is allowed. The periodic boundary conditions are imposed via coupling the degrees of freedom of nodes at boundary edges of the lattices with the corresponding reference points.
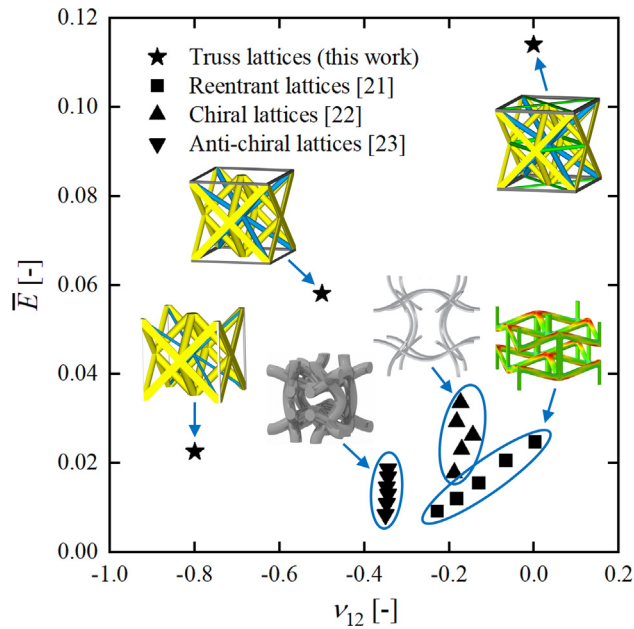
**Fig. 7.** The normalized Young's modulus versus Poisson's ratio within $x$-$y$ plane of the proposed stretching-dominated truss lattices with tailored zero/negative Poisson's ratios and their bending-dominated counterparts in previous studies.

### 3.2. FEA results of elastic constants

The FEA evaluated elastic constants of the designed lattices are listed in Table 6. The degree of anisotropy of the lattices is measured by the universal anisotropy index $A^U$ [44,45]. For the lattices with $\bar{\rho} = 10\%$ designed from transversely isotropic base materials, the FEA results show that Iso-1, Iso-2 lattices possess nearly isotropic elasticity, with the universal anisotropy indexes $A^U$ of $2.393 \times 10^{-5}$, $1.411 \times 10^{-3}$, respectively. They also possess nearly the same normalized Young's moduli, which match well with the theoretical value of 0.165. ZPR, NPR-1, NPR-2 lattices nearly obtain the tailored Poisson's ratios ($v_{12} = v_{21}$) of 0, $-0.5$, $-0.8$, respectively, with the relative errors lower than 10%. Ani-1, Ani-2 lattices nearly obtain the tailored axial Young's moduli ratios ($\bar{E}_1/\bar{E}_3 = \bar{E}_2/\bar{E}_3$) of 2.0, 0.5, respectively, with the relative errors

lower than 4%. The FEA results show that all designed lattices nearly obtain the target elastic properties. The remaining discrepancies between the theoretical and numerical elastic properties are primarily attributed to the bending effects of the lattices, which lead to uneven distribution of normal stresses at different locations of a cross section. To mitigate the influence of bending effects, the elastic constants of the designed lattices with a lower relative density of $\bar{\rho} = 1\%$ are investigated and listed in Table 6. The lattices possess the same topological configurations as those in Fig. 2, Fig. 4, Fig. 6, and the cross-sectional radii of the bars are obtained through dividing those in Table 3, Table 4, and Table 5 by a factor of $\sqrt{10}$. The FEA results imply that the elastic properties of the designed lattices with 1% relative density are much closer to the target values (with relative errors lower than 1%) than those with 10% relative density, due to the lower bending effects.

For the lattices with $\bar{\rho} = 10\%$ designed from isotropic base materials, the FEA evaluated elastic constants deviate more from their target values, due to the assumption of an unrealistic, namely isotropic, base material in the design method. The universal anisotropy indexes $A^U$ of Iso-1, Iso-2 lattices are $4.035 \times 10^{-3}$, $9.169 \times 10^{-3}$, respectively, which are larger than those of Iso-1, Iso-2 lattices designed from transversely isotropic base materials and imply a larger degree of anisotropic elasticity. The FEA evaluated axial Young's moduli ratios ($\bar{E}_1/\bar{E}_3 = \bar{E}_2/\bar{E}_3$) of Ani-1, Ani-2 lattices, and Poisson's ratios within $x$-$y$ plane ($v_{12} = v_{21}$) of ZPR, NPR-1, NPR-2 lattices also deviate more from the target values than those designed from transversely isotropic materials. Such deviations decrease with decreasing relative densities as a result of lower bending effects, while they are still larger than the designed lattices considering material anisotropy. The effects on the elastic constants of the designed lattices evaluated through introducing transversely isotropic base materials in FEA depend on the degree of material anisotropy. Since the anisotropy degree of SS316L materials adopted in this work is relatively low, the differences between the FEA evaluated elastic constants of the designed lattices with and without consideration of material anisotropy are also relatively small. Nevertheless, the extension of the proposed design method considering material anisotropy to other base materials with higher anisotropy degrees will show more significant advantages.

The configurations of ZPR, NPR-1, NPR-2 lattices designed from transversely isotropic base materials under uniaxial stress loading

**Table 6**

The FEA evaluated elastic constants of the designed truss lattices with tailored elasticity from transversely isotropic base materials and isotropic base materials.

| Lattice | Transversely isotropic base materials | | Isotropic base materials | |
|---|---|---|---|---|
| | Elastic constant ($\bar{\rho} = 10\%$) | Elastic constant ($\bar{\rho} = 1\%$) | Elastic constant ($\bar{\rho} = 10\%$) | Elastic constant ($\bar{\rho} = 1\%$) |
| Isotropic-1 (Iso-1) | $\bar{E}_1 = \bar{E}_2 = 0.167$, $\bar{E}_3 = 0.167$, $A^U = 2.393 \times 10^{-5}$, | $\bar{E}_1 = \bar{E}_2 = 0.165$, $\bar{E}_3 = 0.165$, $A^U = 4.522 \times 10^{-6}$, | $\bar{E}_1 = \bar{E}_2 = 0.168$, $\bar{E}_3 = 0.158$, $A^U = 4.035 \times 10^{-3}$, | $\bar{E}_1 = \bar{E}_2 = 0.166$, $\bar{E}_3 = 0.156$, $A^U = 4.063 \times 10^{-3}$, |
| Isotropic-2 (Iso-2) | $\bar{E}_1 = \bar{E}_2 = 0.165$, $\bar{E}_3 = 0.168$, $A^U = 1.411 \times 10^{-3}$, | $\bar{E}_1 = \bar{E}_2 = 0.164$, $\bar{E}_3 = 0.166$, $A^U = 1.468 \times 10^{-4}$, | $\bar{E}_1 = \bar{E}_2 = 0.168$, $\bar{E}_3 = 0.162$, $A^U = 9.169 \times 10^{-3}$, | $\bar{E}_1 = \bar{E}_2 = 0.166$, $\bar{E}_3 = 0.161$, $A^U = 9.616 \times 10^{-3}$, |
| Anisotropic-1 (Ani-1) | $\bar{E}_1 = \bar{E}_2 = 0.187$, $\bar{E}_3 = 0.093$, $\frac{\bar{E}_1}{\bar{E}_3} = \frac{\bar{E}_2}{\bar{E}_3} = 2.007$, | $\bar{E}_1 = \bar{E}_2 = 0.184$, $\bar{E}_3 = 0.092$, $\frac{\bar{E}_1}{\bar{E}_3} = \frac{\bar{E}_2}{\bar{E}_3} = 2.000$, | $\bar{E}_1 = \bar{E}_2 = 0.175$, $\bar{E}_3 = 0.086$, $\frac{\bar{E}_1}{\bar{E}_3} = \frac{\bar{E}_2}{\bar{E}_3} = 2.036$, | $\bar{E}_1 = \bar{E}_2 = 0.171$, $\bar{E}_3 = 0.085$, $\frac{\bar{E}_1}{\bar{E}_3} = \frac{\bar{E}_2}{\bar{E}_3} = 2.012$, |
| Anisotropic-2 (Ani-2) | $\bar{E}_1 = \bar{E}_2 = 0.068$, $\bar{E}_3 = 0.131$, $\frac{\bar{E}_1}{\bar{E}_3} = \frac{\bar{E}_2}{\bar{E}_3} = 0.518$, | $\bar{E}_1 = \bar{E}_2 = 0.065$, $\bar{E}_3 = 0.129$, $\frac{\bar{E}_1}{\bar{E}_3} = \frac{\bar{E}_2}{\bar{E}_3} = 0.502$, | $\bar{E}_1 = \bar{E}_2 = 0.066$, $\bar{E}_3 = 0.123$, $\frac{\bar{E}_1}{\bar{E}_3} = \frac{\bar{E}_2}{\bar{E}_3} = 0.534$, | $\bar{E}_1 = \bar{E}_2 = 0.063$, $\bar{E}_3 = 0.122$, $\frac{\bar{E}_1}{\bar{E}_3} = \frac{\bar{E}_2}{\bar{E}_3} = 0.519$, |
| Zero Poisson's Ratio (ZPR) | $v_{12} = v_{21} = 0.009$, | $v_{12} = v_{21} = -2.074 \times 10^{-6}$, | $v_{12} = v_{21} = -0.01$, | $v_{12} = v_{21} = -0.002$, |
| Negative Poisson's Ratio-1 (NPR-1) | $v_{12} = v_{21} = -0.457$, | $v_{12} = v_{21} = -0.496$, | $v_{12} = v_{21} = -0.447$, | $v_{12} = v_{21} = -0.513$, |
| Negative Poisson's Ratio-2 (NPR-2) | $v_{12} = v_{21} = -0.721$. | $v_{12} = v_{21} = -0.792$. | $v_{12} = v_{21} = -0.716$. | $v_{12} = v_{21} = -0.789$. |
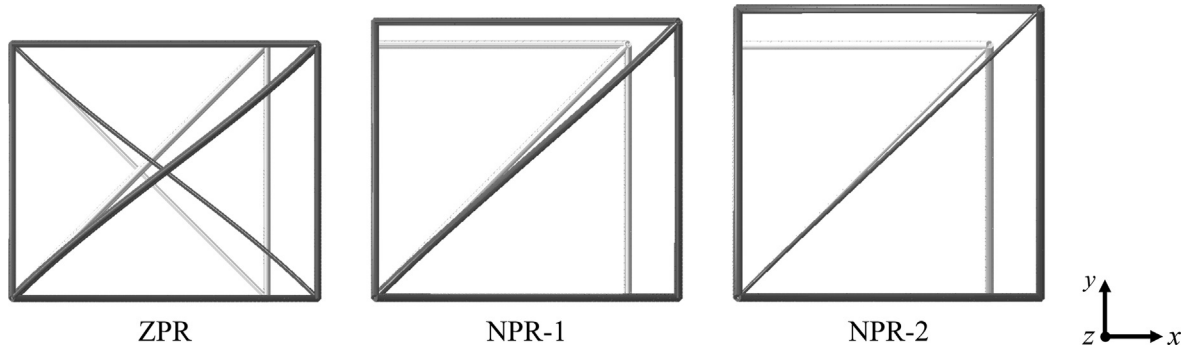
**Fig. 8.** The configurations of ZPR, NPR-1, NPR-2 lattices within the 1/8 unit cell under uniaxial stress loading along *x* direction, in which the white and grey colours represent the undeformed and deformed configurations of the lattices, respectively.

along *x* direction are illustrated in Fig. 8, in which the 1/8 unit cell is adopted for illustration. The white and grey colours represent the undeformed and deformed configurations of the lattices, respectively. The ZPR lattice does not deform along *y* direction when it is subjected to tension along *x* direction, implying zero Poisson's ratio within *x-y* plane. The NPR-1, NPR-2 lattices expand along *y* direction when subjected to tension along *x* direction, implying negative Poisson's ratios within *x-y* plane. Given the same longitudinal strain along *x* direction, the deformation of NPR-2 lattice along *y* direction is larger than that of NPR-1 lattice, since NPR-2 lattice possesses a lower Poisson's ratio within *x-y* plane (-0.8) than NPR-1 lattice (-0.5).

## 4. Experimental validation

### 4.1. Micro-LPBF fabrication

The proposed Iso-1, ZPR and NPR-1 lattices were selected for fabrication and experimental tests to further validate their unconventional properties of isotropic elasticity, tailored zero/negative Poisson's ratios. The lattices were fabricated by a micro-LPBF system Hans' Laser M100 machine, with gas atomized austenitic stainless steel SS316L powders from Beijing AMC Powders Co., Ltd. A 500 W IPG fiber laser was equipped in the machine, and the wavelength and beam diameter were 1.07 μm and 25 μm, respectively; and the SS316L powder size ranged from 5 to 25 μm with $D_{50} = 16.27\ \mu\boldsymbol{m}$. The scanning patterns between sequential layers were rotated by 67° (the hatch angle) to reduce the thermal stresses in the fabrication process and generate nearly homogeneous microstructures throughout the samples [46]. The laser power, hatch distance, layer thickness, scanning speed were set as 50 W, 50 μm, 10 μm and 1000 mm/s, respectively. Such process parameters were selected to ensure dense and pore-free samples based on our previous study [47]. After the micro-LPBF fabrication process, all samples were removed from the substrate baseplate via electrical discharge wire cutting and cleaned with ethanol via ultrasonic vibrations, in which no heat treatment was involved.

### 4.2. Sample configuration and surface morphology characterization

The micro-LPBF fabricated multi-cell samples of the selected lattices with the relative density of $\bar{\rho} = 10\%$ and their fabrication orientations on the baseplate are shown in Fig. 9. The designed and measured geometric properties of the samples are listed in Table 7. Iso-1 lattice was fabricated along the three principal lattice directions of [1 0 0], [1 1 0], [1 1 1], respectively, and ZPR, NPR-1 lattices were fabricated along [1 0 0] direction. Given the minimum

printing feature size of 70 $\boldsymbol{\mu m}$, the unit cell size of the lattices was taken as $D = 2.4\ \boldsymbol{mm}$ to ensure the fabrication accuracy. In view of the transverse isotropy of the base materials, the lattice direction [0 0 1] of all samples was aligned with the material direction (0, 0, 1) within the global coordinate system, while the 'Iso-1 [1 1 1]' sample was rotated along [0 0 1] direction to save the fabrication space. For each designed lattice, 3 samples were fabricated to ensure the experimental repeatability, leading to 15 samples in total. Afterwards, the relative densities of the samples were calculated based on the measured weight and the density of SS316L ($\rho_s = 7.98\ \boldsymbol{g}/\boldsymbol{cm^3}$). The measured relative densities of the samples are slightly larger than the designed values, with the relative errors lower than 20%. The larger relative density results are primarily attributed to the larger cross-sectional radii of the fabricated samples than the designed values. The measured relative densities of the samples within the same group exhibit low standard deviations, implying good repeatability of the micro-LPBF fabrication.

The different constitutive bars can be simultaneously fabricated by the micro-LPBF process in this work, while the fabrication quality of different bars is different. To illustrate this point, the fabricated samples were further inspected by a JSM-7800F Schottky Field Emission Scanning Electron Microscope (FE-SEM), and an RH-2000 High-Resolution 3D Optical Microscope, to characterize their surface morphologies and the cross-section dimensions of the bars. The SEM characterized top and side surfaces of 'Iso-1 [1 0 0]' sample are shown in Fig. 10, and the microscopic surface morphologies and roughness (*Ra*) measured by the 3D optical microscope are shown in Fig. 11. The side surface is found to have more partially-melted loose powders attached than the top surface, leading to a higher roughness of 10.60 μm. In contrast, the top surface exhibits a lower surface roughness of 3.32 μm and possesses better surface finish. The designed cross-sectional radii of the bars in group I, II are 155.52 μm, 162.48 μm, respectively. As comparison, the measured radii are 162.74 μm, 183.07 μm, which are nearly 4.64%, 12.67% larger than the designed values, respectively. Therefore, the micro-LPBF fabricated bars are generally thicker than the designed ones; and vertical bars are thicker than horizontal bars with the same designed cross-sectional radii, since the powders of horizontal bars are easier to be scraped away during powder recoating.

The SEM characterized top and side surfaces of the ZPR sample are shown in Fig. 12. The side surface also shows a larger surface roughness and worse surface finish than the top surface. The fabrication quality of the ZPR sample is lower than 'Iso-1 [1 0 0]' sample, since the ZPR sample possesses more horizontal bars with smaller cross-sectional radii. The ZPR sample possesses more warped horizontal bars, among which some are non-uniform along axial directions or locally broken, since the powders are scraped away during powder recoating. Larger fabrication defects, including surface
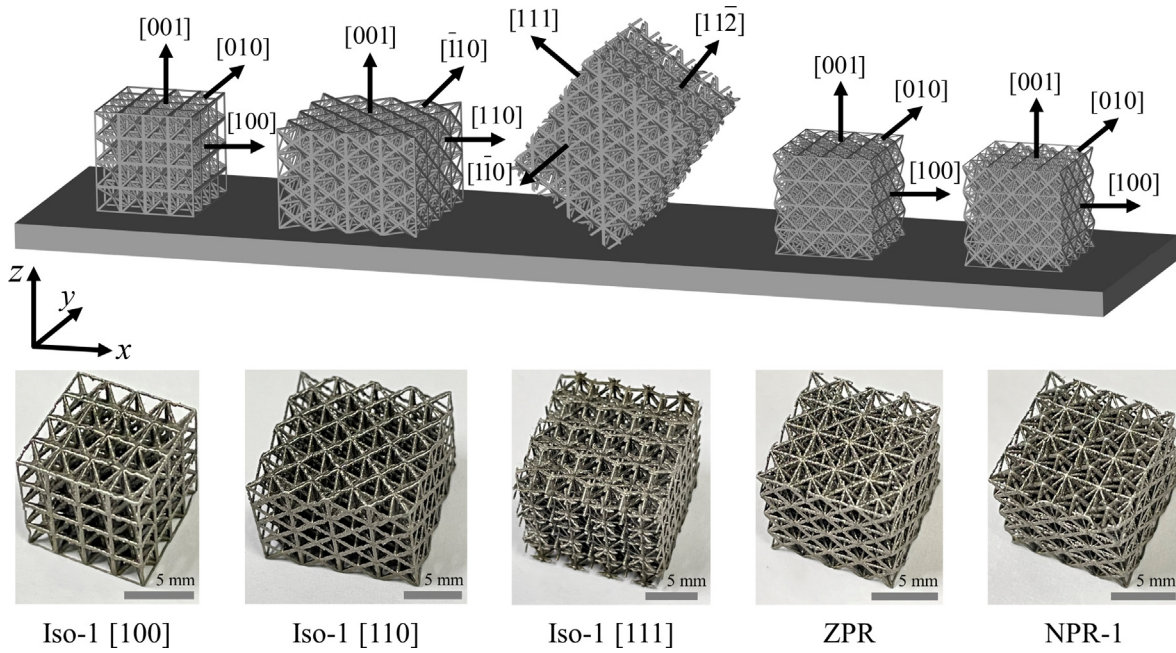
**Fig. 9.** Micro-LPBF fabricated multi-cell samples of the selected truss lattices and their fabrication orientations, in which the arrows denote the lattice directions.

**Table 7**
The designed and measured geometric properties of the samples.

| Sample | Unit cell size $D_1 \times D_2 \times D_3$ [mm] | Number of unit cells | Total size $L_1 \times L_2 \times L_3$ [mm] | Relative density [-] | |
|---|---|---|---|---|---|
| | | | | Designed | Measured |
| Isotropic-1 [100] (Iso-1 [100]) | $2.40 \times 2.40 \times 2.40$ | $4 \times 4 \times 4$ | $9.60 \times 9.60 \times 9.60$ | 10% | $10.22 \pm 0.20\%$ |
| Isotropic-1 [110] (Iso-1 [110]) | $3.39 \times 3.39 \times 2.40$ | $4 \times 4 \times 4$ | $13.58 \times 13.58 \times 9.60$ | | $10.50 \pm 0.32\%$ |
| Isotropic-1 [111] (Iso-1 [111]) | $4.16 \times 3.39 \times 5.88$ | $3 \times 4 \times 2.5$ | $12.47 \times 13.58 \times 14.70$ | | $10.40 \pm 0.15\%$ |
| Zero Poisson's Ratio (ZPR) | $2.40 \times 2.40 \times 2.40$ | $4 \times 4 \times 4$ | $9.60 \times 9.60 \times 9.60$ | | $12.04 \pm 0.22\%$ |
| Negative Poisson's Ratio-1 (NPR-1) | $2.40 \times 2.40 \times 2.40$ | $4 \times 4 \times 4$ | $9.60 \times 9.60 \times 9.60$ | | $10.86 \pm 0.16\%$ |

(a)



(b)
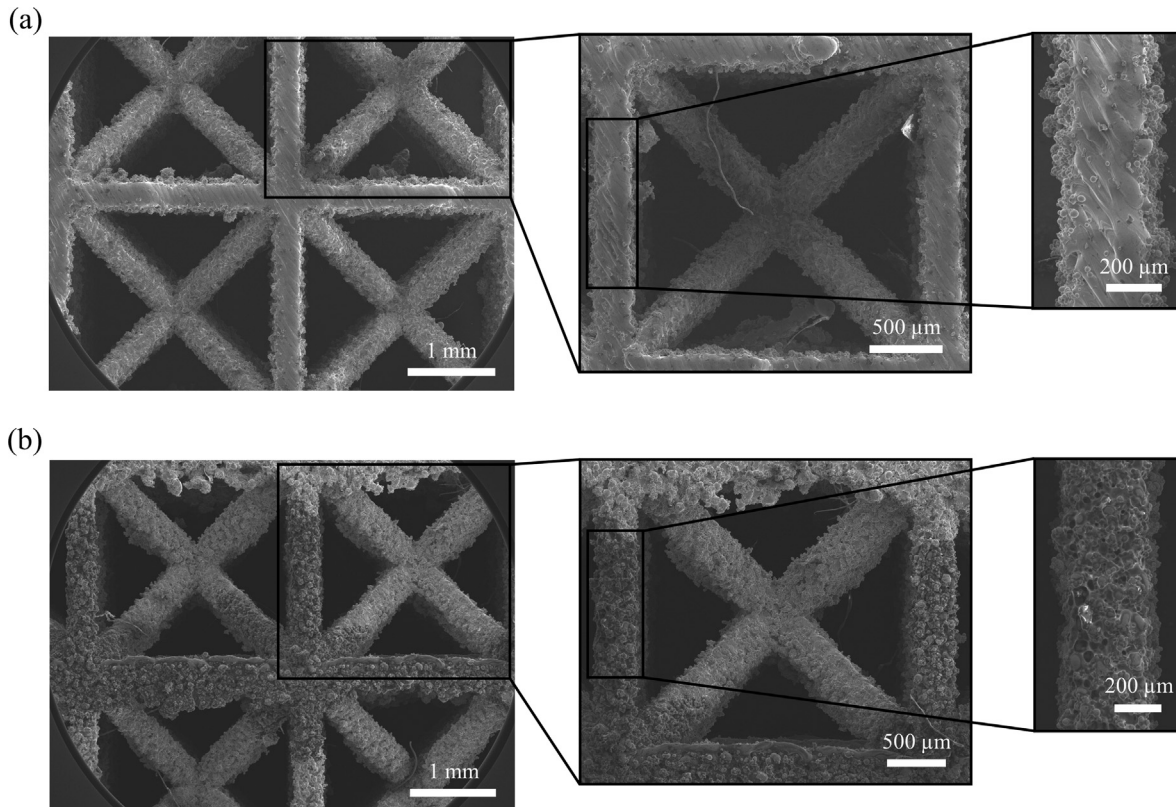


**Fig. 10.** The SEM micrographs of surface morphologies of 'Iso-1 [100]' sample: (a) top surface, (b) side surface.

(a) Top: $Ra$ 3.32 ± 1.29 μm   (b) Side: $Ra$ 10.60 ± 2.07 μm
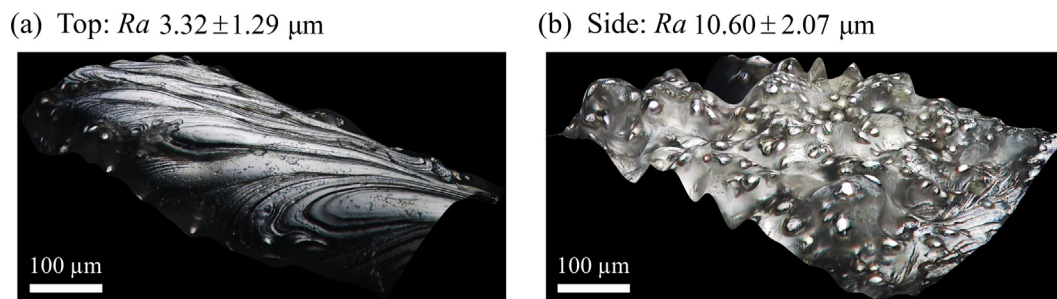


**Fig. 11.** The surface morphologies and roughness measured by the 3D optical microscope for the (a) top, and (b) side surfaces of the 'Iso-1 [1 0 0]' sample.
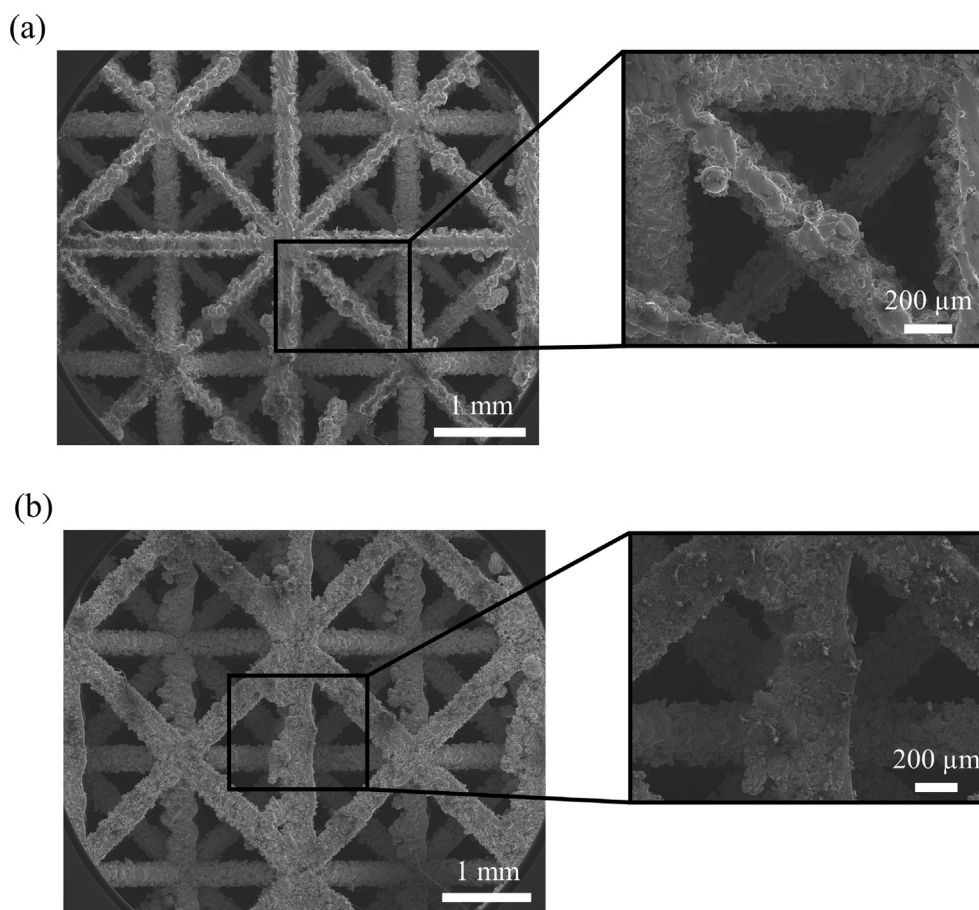


**Fig. 12.** The SEM micrographs of surface morphologies of ZPR sample: (a) top surface, (b) side surface.

roughness, dimensional variations, warping and broken bars, will have larger effects on the measured elastic constants of the ZPR sample.

### 4.3. Experimental validation with compression tests

To measure the elastic constants of micro-LPBF fabricated samples, the uniaxial compression tests were performed using the Tinius Olsen H5KS compression testing machine (with a load cell of 5 kN). All samples were loaded up to 250 N to ensure that they were always in the linear elastic regime. The speed in displacement control mode was set as 0.5 mm/min, which corresponded to the strain rate $(6.14 \sim 8.68) \times 10^{-4}$ /s. The samples 'Iso-1 [1 0 0]', 'Iso-1 [1 1 0]', 'Iso-1 [1 1 1]' were loaded along [1 0 0], [1 1 0], [1 1 1] direc-

tions, respectively, and the samples ZPR, NPR-1 were loaded along [1 0 0] direction. Normally, the first loading curve deviated from the rest of curves as the contact surfaces between the samples and fixtures were not flat in the first loading; while the second and following curves were close to each other [28]. Therefore, the compression tests were performed for four times along each direction, and the elastic constants were calculated based on the average data of the second to the fourth curves.

To accurately measure the Young's moduli of the samples, an additional compression test was performed on the machine (without samples) for four times to measure the stiffness of the machine, since the machine also underwent elastic deformations during the loading. The total stiffness of the machine and sample ($k_{m+s}$), and the stiffness of the machine ($k_m$), were calculated as the average

slope of the second to fourth force–displacement curves of the corresponding tests, from which the Young's modulus of the sample was calculated as [28]:

$$E = \frac{h k_m k_{m+s}}{A_0(k_m - k_{m+s})},\tag{23}$$

where $h$ and $A_0$ denote the height and cross-sectional area of the sample, respectively. Given the differences in relative densities of the fabricated samples, the normalized Young's moduli $\bar{E}$ were calculated and compared with each other to verify the isotropic elasticity of the samples.

To measure the Poisson's ratios, the uniaxial compression test was performed on the ZPR, NPR-1 samples along [100] direction. The deformation history of the samples was recorded by a Sony Alpha 57 camera, with a frequency of 0.5 Hz. For each sample, 8 pairs of nodes were marked to measure the original and deformed lengths along [100], [010] directions, including 4 pairs along [100] direction (blue color), and 4 pairs along [010] direction (green color), as illustrated in Fig. 13. The longitudinal strain ($\varepsilon_x$), transverse strain ($\varepsilon_y$) were calculated as the average of the deformation to original length ratios along [100], [010] directions of the 4 pairs of nodes, respectively, based on which the Poisson's ratio within $x$-$y$ plane $v_{12}$ was evaluated as:

$$v_{12} = -\frac{\varepsilon_y}{\varepsilon_x}.\tag{24}$$

The designed and measured elastic constants of the samples are listed in Table 8. The measured normalized Young's moduli of Iso-1 samples reach nearly 70 ∼ 90% of the theoretical values. Among [100], [110], [111] directions, Iso-1 samples exhibit the lowest and highest Young's moduli along [111] and [110] directions, respectively. The lowest to highest normalized moduli ratio is $\bar{E}_{\min}/\bar{E}_{\max} = \bar{E}_{[111]}/\bar{E}_{[110]} = 0.824$, implying that the isotropic elasticity is almost achieved, with the relative moduli deviation of nearly 18%. The measured Poisson's ratios within $x$-$y$ plane ($v_{12}$) of ZPR, NPR-1 samples are 0.130, −0.445, which almost achieved the design targets of zero and negative (-0.5) Poisson's ratios within $x$-$y$ plane, respectively.
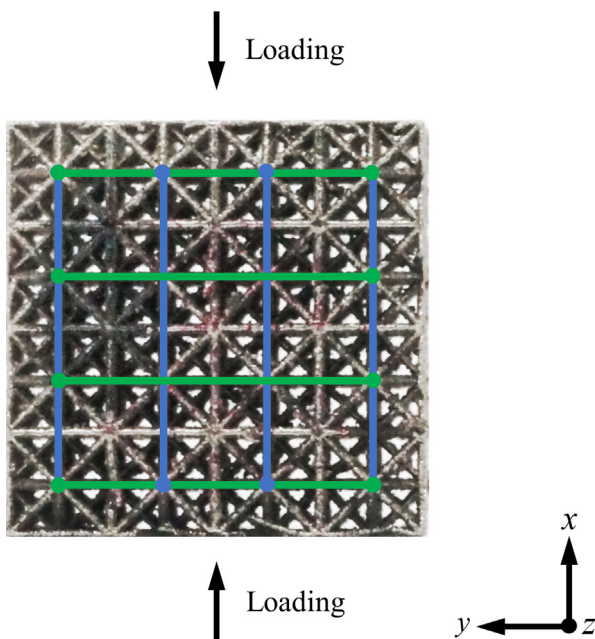
**Table 8**
The theoretical and experimental elastic constants of the samples.

| Sample | Theoretical values | Experimental values |
|---|---|---|
| Isotropic-1 [100] (Iso-1 [100]) | $\bar{E}_{[100]} = 0.165$ | $\bar{E}_{[100]} = 0.140 \pm 0.006$ |
| Isotropic-1 [110] (Iso-1 [110]) | $\bar{E}_{[110]} = 0.165$ | $\bar{E}_{[110]} = 0.147 \pm 0.002$ |
| Isotropic-1 [111] (Iso-1 [111]) | $\bar{E}_{[111]} = 0.165$ | $\bar{E}_{[111]} = 0.121 \pm 0.003$ |
| Zero Poisson's Ratio (ZPR) | $v_{12} = 0$ | $v_{12} = 0.130 \pm 0.005$ |
| Negative Poisson's Ratio-1 (NPR-1) | $v_{12} = -0.5$ | $v_{12} = -0.445 \pm 0.018$ |

In summary, the experimental results are in reasonable agreement with the theoretical values, implying that the tailored isotropic elasticity, and tailored zero/negative Poisson's ratios within $x$-$y$ plane ($v_{12}$) of the designed lattices are nearly obtained. The remaining discrepancies between the experimental and theoretical values are primarily attributed to the fabrication defects [48–50], including dimensional variations, surface roughness and waviness, warping and local fracture of bars. The effects of these defects will be characterized through experimental tests in our future works, based on which the relevant design compensation can be incorporated into the analytical design model to achieve better agreements between the designed properties and actual ones.

## 5. Conclusions

This work proposes an analytical method to design stretching-dominated truss lattices with tailored elastic properties, including isotropic elasticity, tailored zero/negative Poisson's ratios, tailored Young's moduli ratios along specified directions. The transversely isotropic elasticity model is adopted to represent the process-induced anisotropy of the base materials. The lattices are designed through combination of five groups of bars within the cubic lattices of SC, BCC, FCC families. An analytical homogenization theory is formed to obtain the elastic constants of combined lattices. A set of analytical criteria are derived to obtain truss lattices with isotropic elasticity from transversely isotropic materials. Besides, a traversal searching method is developed to determine the ranges of Young's moduli, Poisson's ratios of the lattices, and find the most manufacturable ones with tailored Young's moduli ratios and Poisson's ratios.

The analytical criteria show that the combined lattices possess the same Young's modulus, whose value only depends on the three axial Young's moduli ($E_I$, $E_{II}$, $E_{III}$), and identical Poisson's ratio 0.25, once the isotropic elasticity is obtained. The traversal searching reveals the two Poisson's ratios within $x$-$y$ plane ($v_{12}$, $v_{21}$) may be negative, zero, or positive, while the other four ones are always positive. Accordingly, several representative lattices with tailored Poisson's ratios within $x$-$y$ plane of 0, −0.5, −0.8, and tailored axial Young's moduli ratios ($\bar{E}_1/\bar{E}_3 = \bar{E}_2/\bar{E}_3$) of 2.0 and 0.5, are obtained, respectively. The FEA results reveal that all designed lattices nearly obtain the target elastic properties, and the discrepancies decrease as the relative density decreases. The FEA results also validate the superiority of the proposed design method considering material anisotropy, which leads to designed lattices with closer elastic properties to the target values than those designed without consideration of material anisotropy.

Finally, the Iso-1, ZPR, and NPR-1 lattices are fabricated via micro-LPBF, and their isotropic elasticity, and tailored zero/negative Poisson's ratios are validated via quasi-static compression test experiments. The experimental results agree with theoretical values reasonably, with the target elastic properties almost achieved, and the remaining discrepancies are primarily attributed to the fabrication defects. The characterization and minimization meth-

**Fig. 13.** The graphical interpretation for measurement of Poisson's ratios within $x$-$y$ plane of lattices.

ods for these defects will be investigated in our future works to achieve better agreements between the designed properties and actual ones. Besides, the lattices may exhibit different stress–strain behaviours in large deformations, due to their different topologies and bar arrangements, which also deserves more in-depth investigations in our future studies.

## Data availability

Data will be made available on request.

## Declaration of Competing Interest

The authors declare that they have no known competing financial interests or personal relationships that could have appeared to influence the work reported in this paper.

## Acknowledgements

## Appendix A

Given the compliance matrix $\boldsymbol{S}^b$ of the transversely isotropic materials in Eq. (1), the Young's modulus along the direction $\boldsymbol{n} = (n_1, n_2, n_3)$ can be derived via coordinate transformation [51]. The global coordinate system (O − $xyz$) and local coordinate system (O − $x'y'z'$) are shown in Fig. A1, in which the compliance matrix $\boldsymbol{S}^b$ is represented in global coordinate system, and the $x'$ axis of local coordinate system is aligned with the unit vector $\boldsymbol{n}$. The coordinate transformation between the global and local coordinate systems can be performed through rotating the global coordinate system along $\boldsymbol{N}$ direction for an angle of $\theta$, in which:

$$\boldsymbol{N} = (N_1, N_2, N_3) = \frac{\mathbf{e}_x \times \mathbf{n}}{\|\mathbf{e}_x \times \mathbf{n}\|} = \left(0, -\frac{n_3}{\sqrt{n_2^2 + n_3^2}}, \frac{n_2}{\sqrt{n_2^2 + n_3^2}}\right),$$

$$\theta = \arccos(\mathbf{e}_x \cdot \mathbf{n}) = \arccos(n_1). \tag{A1}$$

The corresponding coordinate transformation matrix is [51]:

$$\mathbf{T} = \begin{bmatrix} l_1 & m_1 & q_1 \\ l_2 & m_2 & q_2 \\ l_3 & m_3 & q_3 \end{bmatrix}, \tag{A2}$$

where:

$$l_1 = N_1^2(1 - \cos\theta) + \cos\theta, \ m_1 = N_1 N_2(1 - \cos\theta) + N_3 \sin\theta,$$
$$q_1 = N_1 N_3(1 - \cos\theta) - N_2 \sin\theta,$$
$$l_2 = N_1 N_2(1 - \cos\theta) - N_3 \sin\theta, \ m_2 = N_2^2(1 - \cos\theta) + \cos\theta,$$
$$q_2 = N_2 N_3(1 - \cos\theta) + N_1 \sin\theta,$$
$$l_3 = N_1 N_3(1 - \cos\theta) + N_2 \sin\theta, \ m_3 = N_2 N_3(1 - \cos\theta) - N_1 \sin\theta,$$
$$q_3 = N_3^2(1 - \cos\theta) + \cos\theta. \tag{A3}$$

The corresponding strain vector transformation matrix is [51]:

$$\mathbf{T}_\varepsilon = \begin{bmatrix} \mathbf{B}_{11} & \mathbf{B}_{12} \\ 2\mathbf{B}_{21} & \mathbf{B}_{22} \end{bmatrix}, \tag{A4}$$

where:

$$\mathbf{B}_{11} = \begin{bmatrix} l_1^2 & m_1^2 & q_1^2 \\ l_2^2 & m_2^2 & q_2^2 \\ l_3^2 & m_3^2 & q_3^2 \end{bmatrix}, \ \mathbf{B}_{12} = \begin{bmatrix} m_1 q_1 & l_1 q_1 & l_1 m_1 \\ m_2 q_2 & l_2 q_2 & l_2 m_2 \\ m_3 q_3 & l_3 q_3 & l_3 m_3 \end{bmatrix},$$

$$\mathbf{B}_{21} = \begin{bmatrix} l_2 l_3 & m_2 m_3 & q_2 q_3 \\ l_1 l_3 & m_1 m_3 & q_1 q_3 \\ l_1 l_2 & m_1 m_2 & q_1 q_2 \end{bmatrix}, \tag{A5}$$

$$\mathbf{B}_{22} = \begin{bmatrix} m_2 q_3 + m_3 q_2 & q_2 l_3 + q_3 l_2 & m_2 l_3 + m_3 l_2 \\ m_3 q_1 + m_1 q_3 & q_3 l_1 + q_1 l_3 & m_3 l_1 + m_1 l_3 \\ m_1 q_2 + m_2 q_1 & q_1 l_2 + q_2 l_1 & m_1 l_2 + m_2 l_1 \end{bmatrix}.$$

Based on the strain vector transformation matrix in Eq. (A4), the compliance matrix $\left(\boldsymbol{S}^b\right)'$ within local coordinate system is derived as [51]:

$$\left(\boldsymbol{S}^b\right)' = \mathbf{T}_\varepsilon \boldsymbol{S}^b \mathbf{T}_\varepsilon^{\boldsymbol{T}}, \tag{A6}$$

from which the Young's modulus along $\boldsymbol{n}$ direction is obtained:



O-*xyz*: global coordinate system

O-*x'y'z'*: local coordinate system

**Fig. A1.** The graphical interpretation of the global and local coordinate systems.

$$E_n^b = \frac{1}{\left(\mathbf{S}^b\right)'_{11}}$$

$$= 1/\left[\frac{1}{E_1^b}\left(l_1^2 + m_1^2\right)\left(l_1^2 + m_1^2 - 2v_{13}^b q_1^2\right) + \frac{1}{E_3^b}q_1^4 + \frac{1}{G_{13}^b}q_1^2\left(l_1^2 + m_1^2\right)\right].$$

$$(A7)$$

Through combination with Eqs. (A1) and (A3), the Young's modulus in Eq. (A7) is further simplified as:

$$E_n^b = 1/\left[\frac{1}{E_1^b}\left(n_1^2 + n_2^2\right)\left(n_1^2 + n_2^2 - 2v_{13}^b n_3^2\right) + \frac{1}{E_3^b}n_3^4 + \frac{1}{G_{13}^b}n_3^2\left(n_1^2 + n_2^2\right)\right],$$

$$(A8)$$

which exactly represents the formula in Eq. (2).

## References

[1] L.J. Gibson, Cellular solids, MRS Bull. 28 (4) (2003) 270–274.
[2] R.G. Hutchinson, N.A. Fleck, The structural performance of the periodic truss, J. Mech. Phys. Solids 54 (4) (2006) 756–782.
[3] T. Buckmann, N. Stenger, M. Kadic, J. Kaschke, A. Frolich, T. Kennerknecht, C. Eberl, M. Thiel, M. Wegener, Tailored 3D mechanical metamaterials made by dip-in direct-laser-writing optical lithography, Adv. Mater. 24 (20) (2012) 2710–2714.
[4] G. Campoli, M. Borleffs, S.A. Yavari, R. Wauthle, H. Weinans, A.A. Zadpoor, Mechanical properties of open-cell metallic biomaterials manufactured using additive manufacturing, Mater. Des. 49 (2013) 957–965.
[5] C. Li, H. Lei, Z. Zhang, X. Zhang, H. Zhou, P. Wang, D. Fang, Architecture design of periodic truss-lattice cells for additive manufacturing, Addit. Manuf. 34 (2020) 101172.
[6] K. Wei, Y. Peng, K. Wang, S. Duan, X. Yang, W. Wen, Three dimensional lightweight lattice structures with large positive, zero and negative thermal expansion, Compos. Struct. 188 (2018) 287–296.
[7] M.A. El-Sayed, K. Essa, M. Ghazy, H. Hassanin, Design optimization of additively manufactured titanium lattice structures for biomedical implants, J. Adv. Manuf. Technol. 110 (9) (2020) 2257–2268.
[8] J. Feng, B. Liu, Z. Lin, J. Fu, Isotropic octet-truss lattice structure design and anisotropy control strategies for implant application, Mater. Des. 203 (2021) 109595.
[9] A. Maiti, W. Small, J.P. Lewicki, T.H. Weisgraber, E.B. Duoss, S.C. Chinn, M.A. Pearson, C.M. Spadaccini, R.S. Maxwell, T.S. Wilson, 3D printed cellular solid outperforms traditional stochastic foam in long-term mechanical response, Sci. Rep. 6 (1) (2016) 1–9.
[10] V.S. Deshpande, M.F. Ashby, N.A. Fleck, Foam topology: bending versus stretching dominated architectures, Acta Mater. 49 (6) (2001) 1035–1040.
[11] V.S. Deshpande, N.A. Fleck, M.F. Ashby, Effective properties of the octet-truss lattice material, J. Mech. Phys. Solids 49 (8) (2001) 1747–1769.
[12] T. Tancogne-Dejean, D. Mohr, Stiffness and specific energy absorption of additively-manufactured metallic BCC metamaterials composed of tapered beams, Int. J. Mech. Sci. 141 (2018) 101–116.
[13] D. Qi, H. Yu, M. Liu, H. Huang, S. Xu, Y. Xia, G. Qian, W. Wu, Mechanical behaviors of SLM additive manufactured octet-truss and truncated-octahedron lattice structures with uniform and taper beams, Int. J. Mech. Sci. 163 (2019) 105091.
[14] N. Francois, M.T. Arnoux, L. Garcia, S.T. Hyde, V. Robins, M. Saadatfar, M. Saba, T.J. Senden, Experimental investigation of the mechanical stiffness of periodic framework-patterned elastomers, Philos. Trans. Royal Soc. A 372 (2008) (2014) 20120035.
[15] T. Tancogne-Dejean, D. Mohr, Elastically-isotropic truss lattice materials of reduced plastic anisotropy, Int. J. Solids Struct. 138 (2018) 24–39.
[16] Q. Ma, Z. Yan, L. Zhang, M.Y. Wang, The family of elastically isotropic stretching-dominated cubic truss lattices, Int. J. Solids Struct. 239-240 (2022) 111451.
[17] Z. Hashin, S. Shtrikman, A variational approach to the theory of the elastic behaviour of multiphase materials, J. Mech. Phys. Solids 11 (2) (1963) 127–140.
[18] R.M. Christensen, Mechanics of low density materials, J. Mech. Phys. Solids 34 (6) (1986) 563–578.
[19] S. Wang, Y. Ma, Z. Deng, Stretching-dominated truss lattice materials: Elastic anisotropy evaluation, control, and design, Compos. Struct. 298 (2022) 116004.
[20] S. Wang, Y. Ma, Z. Deng, X. Wu, Two elastically equivalent compound truss lattice materials with controllable anisotropic mechanical properties, Int. J. Mech. Sci. 213 (2022) 106879.
[21] G. Tzortzinis, A. Gross, S. Gerasimidis, Auxetic boosting of confinement in mortar by 3D reentrant truss lattices for next generation steel reinforced concrete members, Extreme Mech. Lett. 52 (2022) 101681.
[22] F. Warmuth, F. Osmanlic, L. Adler, M.A. Lodes, C. Körner, Fabrication and characterisation of a fully auxetic 3D lattice structure via selective electron beam melting, Smart Mater. Struct. 26 (2) (2017) 025013.
[23] F. Albertini, J. Dirrenberger, C. Sollogoub, T. Maconachie, M. Leary, A. Molotnikov, Experimental and computational analysis of the mechanical properties of composite auxetic lattice structures, Addit. Manuf. 47 (2021) 102351.
[24] Y. Gao, X. Wei, X. Han, Z. Zhou, J. Xiong, Novel 3D auxetic lattice structures developed based on the rotating rigid mechanism, Int. J. Solids Struct. 233 (2021) 111232.
[25] P. Zhang, J. Liu, A.C. To, Role of anisotropic properties on topology optimization of additive manufactured load bearing structures, Scr. Mater. 135 (2017) 148–152.
[26] Y. Kok, X.P. Tan, P. Wang, M. Nai, N.H. Loh, E. Liu, S.B. Tor, Anisotropy and heterogeneity of microstructure and mechanical properties in metal additive manufacturing: A critical review, Mater. Des. 139 (2018) 565–586.
[27] N. Zohdi, R.C. Yang, Material Anisotropy in Additively Manufactured Polymers and Polymer Composites: A Review, Polymers 13 (19) (2021) 3368.
[28] Q. Ma, L. Zhang, J. Ding, S. Qu, J. Fu, M. Zhou, M.W. Fu, X. Song, M.Y. Wang, Elastically-isotropic open-cell minimal surface shell lattices with superior stiffness via variable thickness design, Addit. Manuf. 47 (2021) 102293.
[29] V. Laghi, L. Tonelli, M. Palermo, M. Bruggi, R. Sola, L. Ceschini, T. Trombetti, Experimentally-validated orthotropic elastic model for wire-and-arc additively manufactured stainless steel, Addit. Manuf. 42 (2021) 101999.
[30] B. Fedulov, A. Fedorenko, A. Khaziev, F. Antonov, Optimization of parts manufactured using continuous fiber three-dimensional printing technology, Compos. B. Eng. 227 (2021) 109406.
[31] G.W. Milton, A. Sawicki, Theory of composites: Cambridge monographs on applied and computational mathematics, Appl. Mech. Rev. 56 (2) (2003) B27–B28.
[32] S. Li, S. Yuan, J. Zhu, C. Wang, J. Li, W. Zhang, Additive manufacturing-driven design optimization: Building direction and structural topology, Addit. Manuf. 36 (2020) 101406.
[33] Y. Wang, S. Li, Y. Yu, Y. Xin, X. Zhang, Q. Zhang, S. Wang, Lattice structure design optimization coupling anisotropy and constraints of additive manufacturing, Mater. Des. 196 (2020) 109089.
[34] D.R. Jantos, K. Hackl, P. Junker, Topology optimization with anisotropic materials, including a filter to smooth fiber pathways, Struct. Multidiscip. Optim. 61 (5) (2020) 2135–2154.
[35] X. Yan, Q. Xu, H. Hua, D. Huang, X. Huang, Concurrent topology optimization of structures and orientation of anisotropic materials, Eng. Optim. 52 (9) (2020) 1598–1611.
[36] Y. Lu, L. Tong, Concurrent topology optimization of cellular structures and anisotropic materials, Compos. Struct. 255 (2021) 106624.
[37] Y. Wu, L. Yang, Modeling and analysis of material anisotropy-topology effects of 3D cellular structures fabricated by powder bed fusion additive manufacturing, Int. J. Mech. Sci. 197 (2021) 106325.
[38] Z.P. Sun, Y.B. Guo, V.P.W. Shim, Characterisation and modeling of additively-manufactured polymeric hybrid lattice structures for energy absorption, Int. J. Mech. Sci. 191 (2021) 106101.
[39] L. Zhang, Q. Ma, J. Ding, S. Qu, J. Fu, M.W. Fu, X.u. Song, M.Y. Wang, Design of elastically isotropic shell lattices from anisotropic constitutive materials for additive manufacturing, Addit. Manuf. 59 (2022) 103185.
[40] Z. Yuan, J. Fish, Toward realization of computational homogenization in practice, Int. J. Numer. Methods Eng. 73 (3) (2008) 361–380.
[41] S. Li, Boundary conditions for unit cells from periodic microstructures and their implications, Compos. Sci. Technol. 68 (9) (2008) 1962–1974.
[42] D.W. Lee, K.A. Khan, R.K.A. Al-Rub, Stiffness and yield strength of architectured foams based on the Schwarz Primitive triply periodic minimal surface, Int. J. Plast. 95 (2017) 1–20.
[43] Q. Ma, L. Zhang, M.Y. Wang, Elastically isotropic open-cell uniform thickness shell lattices with optimized elastic moduli via shape optimization, Mater. Des. 215 (2022) 110426.
[44] D.H. Chung, W.R. Buessem, The elastic anisotropy of crystals, J. Appl. Phys. 38 (5) (1967) 2010–2012.
[45] C.M. Kube, Elastic anisotropy of crystals, AIP Adv. 6 (9) (2016) 095209.
[46] J. Xu, Y. Ding, Y. Gao, H. Wang, Y. Hu, D. Zhang, Grain refinement and crack inhibition of hard-to-weld Inconel 738 alloy by altering the scanning strategy during selective laser melting, Mater. Des. 209 (2021) 109940.
[47] J. Fu, S. Qu, J. Ding, X. Song, M.W. Fu, Comparison of the microstructure, mechanical properties and distortion of stainless steel 316 L fabricated by micro and conventional laser powder bed fusion, Addit. Manuf. 44 (2021) 102067.
[48] L. Liu, P. Kamm, F. García-Moreno, J. Banhart, D. Pasini, Elastic and failure response of imperfect three-dimensional metallic lattices: the role of geometric defects induced by Selective Laser Melting, J. Mech. Phys. Solids 107 (2017) 160–184.
[49] L. Zhang, J. Lifton, Z. Hu, R. Hong, S. Feih, Influence of geometric defects on the compression behaviour of thin shell lattices fabricated by micro laser powder bed fusion, Addit. Manuf. 58 (2022) 103038.
[50] J. Ding, S. Qu, L. Zhang, M.Y. Wang, X. Song, Geometric deviation and compensation for thin-walled shell lattice structures fabricated by high precision laser powder bed fusion, Addit. Manuf. 58 (2022) 103061.
[51] M. Bao, Analysis and design principles of MEMS devices, Elsevier, 2005.